



Difunctional Ni₂P decorated novel Z-scheme BiVO₄/g-C₃N₄ heterojunction for achieving highly efficient CO₂ reduction and tetracycline oxidation

Cheng Hu^a, Jing Cao^a, Xuemei Jia^{a,*}, Haoyu Sun^a, Haili Lin^{a,*}, Shifu Chen^{a,*}

^a Key Laboratory of Green and Precise Synthetic Chemistry and Applications, Ministry of Education; College of Chemistry and Materials Science, Huaibei Normal University, Huaibei, Anhui 235000, PR China

ARTICLE INFO

Keywords:
Coupled reaction system
Z-scheme
Difunctional Ni₂P
Electron-bridge
Co-catalyst

ABSTRACT

The Z-scheme heterojunction has great potential in synchronous CO₂ reduction and tetracycline degradation due to its strong redox capacity. However, the high interfacial migration resistance severely restricts its practical application. Herein, a difunctional Ni₂P, as an electron-bridge and co-catalyst, was rationally introduced into the BiVO₄/g-C₃N₄ Z-scheme system to reduce interfacial transfer resistance, which presented a better photocatalytic property than that of BiVO₄/g-C₃N₄ heterojunction. What is more, the difunctional roles of Ni₂P in boosting photocatalytic activity were deeply discussed. Obviously, the metallic Ni₂P, as an electron-bridge could effectively reduce the interfacial migration resistance of electrons, meanwhile, as a co-catalyst on the surface of g-C₃N₄ not only accelerated separation and migration of carriers, but also increased more active sites for CO₂ reduction, thereby, maximizing the separation efficiency of carriers. This work highlighted the synergistic effect of transition metal phosphides electron-bridge and co-catalyst to design efficient photocatalysts for environment and energy applications.

1. Introduction

Environmental pollution and energy issues have become a significant challenge for scientific community and human society today. Up to now, semiconductor photocatalysis has been considered as a promising and effective method to solve the above two difficult problems [1–3]. Particularly, recent surge of photocatalytic CO₂ reduction integrated with organics oxidation synthesis in a redox reaction system delineated a fascinating approach, which enabled the complete utilization of photoinduced carriers [4–7]. Nevertheless, the residual organic solvents and by-products brought secondary pollution, which was difficult for such coupled reaction systems to achieve the purpose of win-win energy and environment. Hence, it is necessary to design a perfect coupled reaction system for simultaneous energy generation and environmental remediation. Draw lessons from the principle of CO₂ reduction coupled with organics oxidation synthesis, acted in a diametrically opposite way to devise a coupled reaction system. Starting from the inverse of oxidative half-reaction, that is, the “traditional fine chemical synthesis” was replaced by “organic pollution mineralization”, which integrated with CO₂ reduction to establish an ideal coupled reaction system. The construction of such coupled reaction system (CO₂ reduction coupled

with pollution removal) not only realized the purpose of win-win results between environment and energy, but also achieved the full utilization of carriers.

To accomplish this photo-redox catalyzed reaction system, it is quite indispensable to legitimately design a high-efficiency photocatalyst with strong redox potential, more surface-active sites and speedy separation rate of carriers. Newly, graphitic carbon nitride (g-C₃N₄) [7–11], as a metal-free semiconductor, has been extensively researched in the field of photocatalysis due to its facile preparation, chemical stability and especially strong reduction potential ($E_{CB} \approx -1.0$ eV) [12]. Nevertheless, the swift recombination rate of carriers and poor quantum efficiency restricted its actual application. Subsequently, a series of tactics have been carried out to address the above-mentioned inherent shortcomings, such as defect engineering [13,14], element doping [15], loading cocatalysts [16], constructing heterostructure [17–19] and adjusting morphology [20]. Among them, the construction of g-C₃N₄-based heterojunctions may be considered as one of the most promising approaches for solving the above problems [9–12]. Among various heterojunctions, type-I heterojunction with embedded band alignment was not conducive to the separation and migration of carriers [21]. Despite the carriers could be effectively separated in type-II

* Corresponding authors.

E-mail addresses: XuemeiJia@njjust.edu.cn (X. Jia), linhaili@mail.ipc.ac.cn (H. Lin), chshifu@chnu.edu.cn (S. Chen).

<https://doi.org/10.1016/j.apcatb.2023.122957>

Received 28 February 2023; Received in revised form 13 May 2023; Accepted 3 June 2023

Available online 5 June 2023

0926-3373/© 2023 Elsevier B.V. All rights reserved.

heterojunctions because of staggered band alignment, the redox ability of carriers was weak [22,23]. By comparison, Z-scheme heterojunctions not only expedited the separation of electrons and holes, but also preserved the strong redox ability of photoinduced carriers [9–12,24], which served as a desired system for photocatalytic energy conversion and contaminants removal. Since g-C₃N₄ with a relatively negative conduction band potential (E_{CB}) was considered as a reduction-type photocatalyst [7,8], which could constitute Z-scheme heterojunction with an oxidation-type photocatalyst.

Recently, BiVO₄, as a typical semiconductor, has gained widespread concerns due to unique layered structure, suitable band gap energy, strong oxidizing ability and good photochemical stability [25–27]. In especial, BiVO₄ as an oxidation-type semiconductor owned more positive E_{CB} , which could form into Z-scheme heterojunctions with a reduction type semiconductor like black phosphorous (BP) [28], CuS [29], Cu₂O [30] and g-C₃N₄ [31–34]. Especially, the Z-scheme heterojunction photocatalyst by modifying BiVO₄ with g-C₃N₄ presented excellent photocatalytic activity for water splitting [31], CO₂ conversion [32], ciprofloxacin removal [33] or tetracycline degradation [34]. Although the construction of BiVO₄/g-C₃N₄ Z-scheme heterojunction could effectively ameliorate the photocatalytic performance, the high interface resistance and limited surficial active sites enormously restricted its actual application [26–29]. Thus, it is highly eager to design an efficient Z-scheme heterojunction.

Recent progresses on the synergetic introduction of electron-bridge and co-catalyst in the heterojunction have indicated this green and ideal approach. For example, Bagherzadeh's group synthesized the Pd-rGO/CNT/CaFe₂O₄ heterojunction with excellent organic pollutants degradation ability due to the synergy effects of CNT electron-bridge and Pd co-catalyst [35]. Jin et al. reported the UiO-66 electron-bridge coupled with WP co-catalyst for efficient visible-light-driven H₂ evolution [36]. Wen et al. recently reported the introduction of Au electron-bridge and Pt co-catalyst in Z-scheme ZnO/g-C₃N₄ heterojunction with excellent photoelectrochemical H₂ evolution [37]. Thus, the introduction of suitable electron-bridge and co-catalyst, as a faultless tactics, was applied to the BiVO₄/g-C₃N₄ Z-scheme heterojunction, which not only reduced the interfacial resistance by utilizing electron-bridge, but also increased surface active sites by using co-catalyst. Up until now, multifarious noble metals (Pt [38], Au [19], and Ag [31]), transition metals (Cd [39] and Cu [40]), and non-metal materials (CDs [25], RGO [10], oxygen defects [41] and MCNTs [42]) have been widely used as electron-bridges or co-catalysts. Nevertheless, they either suffer from low reserves or expensive costs, which enormously limited their practical application. Newly, transition metal phosphides (TMPs) [43–46], due to their low overpotential, high stability, low cost, and outstanding electrical conductivity, have been extensively researched as non-noble metal co-catalyst to increase reaction sites and reduce the overpotential, thereby ameliorating the photocatalytic activity [47,48]. According to the above-mentioned characteristics of TMPs, the TMPs also completely satisfied the requirements of electron-bridge. As a typical representative of TMPs, Ni₂P as electron-bridge could available lower electrons migration resistance at heterojunction interface has been identified by our previous work [49,50]. Besides, Li's group further confirmed that the Ni₂P, as electron migration channel, achieved efficient electrons transfer from g-C₃N₄ to MoS₂, thereby boosting H₂ generation [51]. Thus, if a difunctional Ni₂P, acting both as an electron-bridge and as a co-catalyst, was introduced into the Z-scheme system, which could be an effective strategy to build the ideal Z-scheme system. As far as we know, no previous study has reported the latest application of TMPs both as an electron-bridge and as a co-catalyst in Z-scheme heterojunctions for photo-redox-catalyzed reaction system.

Herein, according to the unique characters of Ni₂P and above ameliorative tactics, we integrated the difunctional Ni₂P into BiVO₄/g-C₃N₄ Z-scheme heterojunction. The difunctional Ni₂P not only served as an electron-bridge between the BiVO₄ and g-C₃N₄, but also acted as a co-

catalyst on the g-C₃N₄ surface for CO₂ reduction, which both reduced the interfacial migration resistance and increased the number of active sites, thereby, maximizing the separation rate of carriers for efficient photocatalytic CO₂ reduction coupled with tetracycline (TC) degradation. Besides, the BiVO₄/Ni₂P/g-C₃N₄ Z-scheme heterojunction obviously advanced the photocatalytic activity of the coupled reaction system (CO₂ reduction coupled with TC degradation), in which the difunctional Ni₂P accelerated the transfer and separation of carriers, meanwhile, the coupled reaction system realized the full utilization of charges. This work provided a novel insight into the application of difunctional TMPs into heterojunctions photocatalysts for high-efficiency CO₂ reduction coupled with contaminants removal.

2. Experimental

2.1. Chemicals

Ammonium metavanadate (NH₄VO₃) and red phosphorus were bought from Aladdin Chemical Reagent Co., Ltd. Bismuth nitrate pentahydrate (Bi(NO₃)₃•5 H₂O), nickel (II) chloride hexahydrate (NiCl₂•6 H₂O), melamine (C₃H₆N₆), nitric acid (HNO₃), sodium hydroxide (NaOH) and tetracycline (TC) were purchased from Sinopharm Chemical Reagent Co., Ltd. All reagents were used without further purification.

2.2. Synthesis of photocatalyst

Preparation of g-C₃N₄ nanorods: Firstly, bulk g-C₃N₄ was prepared through polycondensation of melamine. In brief, 6 g of melamine was put into a crucible and calcinated with a heating rate of 5 °C/min at 550 °C for 4 h in a furnace. The sample was grounded into powders after cooling naturally to ambient temperature. To prepare g-C₃N₄ nanorods, 2.0 g of bulk g-C₃N₄ powders was calcined again similar to bulk g-C₃N₄.

The BiVO₄/g-C₃N₄ heterojunctions were synthesized via hydrothermal method. Typically, 0.097 g of Bi(NO₃)₃•5 H₂O (0.2 mmol) were completely dissolved in 20.0 mL of HNO₃ (2.0 M) solution and then 0.320 g of g-C₃N₄ was added to form homogeneous suspension (A). The solution (B) was obtained by dissolving 0.023 g of NH₄VO₃ (0.2 mmol) into 10 mL of NaOH (2.0 M) aqueous solution under ultrasonic treatment. Subsequently, the solution (B) was added dropwise into the solution (A). 2.0 M NaOH solution was introduced dropwise to in the system until the pH value to 7.0. After successive stirring for 0.5 h, the precipitate was transferred to a 100 mL of Teflon-lined stainless-steel autoclave (Anhui Kemi Machinery Technology Co., Ltd.) and heated at 180 °C for 12 h in an electric oven. The products were collected by washing with ethanol and distilled water, and then dried at 80 °C for about 12 h. Finally, the product was named as 20 wt% BiVO₄/g-C₃N₄ (labeled as 0.2BV/CN). Similarly, a series of xBV/CN composites (x = 0.05, 0.1, 0.2, 0.3, 0.4, which represented the mass ratio of BiVO₄ to g-C₃N₄) were synthesized by changing the amount of g-C₃N₄. For comparison, pure BiVO₄ was fabricated using the above-mentioned process without the addition of g-C₃N₄.

The Ni₂P/g-C₃N₄ composites were fabricated by hydrothermal method. Briefly, 0.05 g of NiCl₂•6 H₂O (0.2 mmol) was dissolved into 40 mL of deionized water. Next, 0.50 g of g-C₃N₄ and 0.06 g of RP were dispersed into the above solution and sonicated for 30 min to form a homogeneous turbid solution. The suspension was transferred to a 100 mL of Teflon-lined stainless-steel autoclave and heated at 140 °C for 10 h in an electric oven. The products were harvested similarly as BiVO₄/g-C₃N₄ heterojunctions. Finally, the product was named as 3 wt% Ni₂P/g-C₃N₄ (labeled as 0.03Ni₂P/CN). Similarly, the yNi₂P/CN composites (y = 0.0075, 0.015, 0.045, 0.06, which stand for the mass ratio of Ni₂P to g-C₃N₄) were prepared by altering the mass of g-C₃N₄. As a contrast, pristine Ni₂P was fabricated using the above-mentioned process without the addition of g-C₃N₄.

The BiVO₄/Ni₂P/g-C₃N₄ composites were prepared by depositing BiVO₄ onto the surface of Ni₂P/g-C₃N₄ composites. Similar to the above-

mentioned synthesis procedure of 0.2BV/CN, the BiVO₄/Ni₂P/g-C₃N₄ composites were also synthesized by replacing the g-C₃N₄ with γ-Ni₂P/CN. The obtained samples were labeled as 0.2BV/γNi₂P/CN (γ = 0.0075, 0.015, 0.03, 0.045, 0.06). The corresponding preparation process of BiVO₄/Ni₂P/g-C₃N₄ sample was presented in Fig. 1a.

As a reference, 0.2BV/0.03Ni₂P was synthesized according to the preparation process of 0.2BV/0.03Ni₂P/CN without the addition of g-C₃N₄.

To investigate the effect of different position of Ni₂P, the 0.2BV/CN/0.03Ni₂P was prepared via depositing the Ni₂P onto the surface of 0.2BV/CN composite. Refer to the synthesis process of 0.03Ni₂P/CN, 0.2BV/CN/0.03Ni₂P was also synthesized by changing the bare g-C₃N₄ to 0.2BV/CN composite. Similar to the synthesis process of 0.2BV/0.03Ni₂P/CN, the 0.2BV/0.03Au/CN was synthesized by replacing Ni₂P with Au.

2.3. Characterizations

The crystal structures of catalysts were detected by a Bruker D8 Advance X-ray diffractometer (XRD). In order to observe the microstructure of the photocatalysts, the ZEISS Sigma 300 scanning electron microscopy (SEM) and the JEOL F200 transmission electron microscopy (TEM) was used. The light absorption properties of photocatalysts were recorded using a Shimadzu UV-3600 iplus UV-vis spectrophotometer (DRS). The reactive radicals were obtained by the Bruker EMX plus paramagnetic resonance spectrometer (ESR). The hydroxyl radicals (•OH) and superoxide radicals (•O₂⁻) were detected utilizing 5,5-dimethyl-1-pyrroline N-oxide (DMPO) as a spin-trapping agent. In brief, 2 mg of photocatalyst was added into 2 mL of DMPO solution (100 mM). The •O₂⁻ and •OH was trapped in methyl alcohol and water medium, respectively, under visible-light irradiation. A 300 W Xe lamp equipped with a UV cut-off filter (λ > 420 nm) as illuminant. Upon irradiation, the mixed solution was measured on ESR device at a given time intervals. The in situ irradiated XPS spectra were analyzed by a PHI5000 Versa Probe III X-ray photoelectron spectrometer (XPS). To measure the specific surface area and CO₂ adsorption of samples, the Micromeritics ASAP2460 surface area analyzer was applied. The Bruker INVENIOR FT-IR spectrometer was used to test in situ FT-IR spectra. Both the steady state photoluminescence (PL) spectra and time-resolved fluorescence (TRPL) decay curves were characterized using the Edinburgh Instruments FLS980 fluorescence spectrometer. Zeta potential was measured using Mano ZS90 Zeta sizer.

2.4. Photocatalytic measurements

A MC-SPB10-AG CO₂ reaction system (Beijing MerryChange Technology Co., Ltd) with a MC-PF300C 300 W Xe lamp equipped with a UV cut-off filter (λ > 420 nm) as illuminant was used to measure the photocatalytic CO₂ reduction coupled with TC oxidation. In order to rapidly reduce the heat emitted by Xe lamp and effectively inhibit the evaporation of H₂O in the reaction system, the temperature of the whole photocatalytic measurement was maintained at 6 °C by circulating the water with condensation. Briefly, the 50 mg of photocatalyst was dispersed by sonication for 5 min in a reactor containing 50.0 mL of 20 mg/L TC aqueous solution. Afterwards, the reactor was mounted on the reaction system and vacuumized. After that, the system was poured 50.0 mL of 99.999 % CO₂ as the react gas. The gas product after light reaction was measured by a Fuli GC9790II (Zhejiang, Fuli Analytical Instruments Co., Ltd) gas chromatograph. And the absorbance of the supernatant after the reaction was measured using a UV-visible spectrophotometer (DRS, Shimadzu, UV-3600 iplus). In addition, the procedure of adsorption isotherm models was presented in Text S1.

The apparent quantum efficiency (AQE) was calculated according to the following formula [52]:

$$\begin{aligned} \text{AQE}(\%) &= \frac{\text{Number of reacted electrons}}{\text{Number of incident photons}} \times 100\% \\ &= \frac{[2 \times n(\text{CO}) + 8 \times n(\text{CH}_4)] \times N_0}{\frac{I \times S \times t}{hc}} \times 100\% \end{aligned}$$

Where $n(\text{CH}_4)$ and $n(\text{CO})$ represented the mole number of CH₄ and CO evolution, respectively. Moreover, N_0 , S , I and t expressed as Avogadro constant, illumination area, light intensity and time, respectively.

2.5. Photoelectrochemical tests

Electrochemical impedance spectrum (EIS), photocurrent responses, and Mott-Schottky (M-S) curves were measured on a CHI 660E electrochemical workstation using 0.5 M Na₂SO₄ solution as electrolyte solution. The counter and reference electrode were platinum plate and Ag/AgCl, respectively. The working electrode was manufactured on the basis of the following steps: Firstly, 3 mg of sample was dispersed into 2 mL of mixture containing ethanol/distilled water/Nafion and sonicated for 30 min to form uniform suspension. Next, 0.2 mL of suspension liquid was sprayed on 1 × 1 cm conductive glass and dried naturally.

2.6. Density functional theory (DFT) calculations

First-principal calculation according to DFT was computed based on the VASP (Vienna Ab initio Simulation Package) means [53,54]. The exchange-correlation potential was adopted through GGA (generalized gradient approximation) function [55,56]. Brillouin zone was selected at a vacuum thickness of 15 Å for the calculations of BiVO₄ (204), g-C₃N₄ (002), and Ni₂P (200), respectively. The configuration was optimized with maximal pressure on each atom below 0.02 eV/Å using 10⁻⁵ eV as the cut-off energy of plane wave.

The adsorption energies (E_{ads}) of substrate on the surface of pure BiVO₄ (204), g-C₃N₄ (002), and Ni₂P (200) and difference sides of BiVO₄/Ni₂P/g-C₃N₄ heterojunction were defined according to $E_{\text{ads}} = E_{\text{tot}} - E_{\text{slab}} - E_{\text{sub}}$, where E_{sub} , E_{slab} , E_{tot} were the energies of independent substrate, clean surface, and substrate adsorbed on the surface, respectively. Besides, the DFT calculation methods on Fukui index of TC was presented in Text S2.

3. Results and discussion

3.1. Characterization of samples

The microstructures of the as-obtained catalysts were firstly observed by SEM, TEM and HRTEM. As we can see from Fig. 1b, pure BiVO₄ presented well-distributed nanospheres, which was composed of massive decahedron crystals. After coupling with Ni₂P (Fig. S1a), it can be found that numerous Ni₂P nanoparticles (Fig. 1c) uniformly dispersed on the surface of BiVO₄ nanospheres. When the g-C₃N₄ nanorods (Fig. 1d) were modified by BiVO₄, the BiVO₄ decahedron crystals were dispersed on the surface of the g-C₃N₄ nanorods (Fig. S1b). As shown in Fig. S2a, the low-magnification TEM images were in accord with the above SEM observation. The HRTEM images of 0.2BV/CN revealed unambiguous lattice spacing of 0.194 nm, assigning to (204) crystal plane of BiVO₄. Moreover, the disordered and dim layer at BiVO₄ edges was identified to amorphous g-C₃N₄ (Fig. S2b). For 0.03Ni₂P/CN, it was displayed in Fig. S3 that some Ni₂P nanoparticles were loaded on the g-C₃N₄ nanorods. After introducing BiVO₄ into the surface of 0.03Ni₂P/CN (Fig. 1e), it could be observed that the decahedron crystal's structure BiVO₄ randomly spread on the surface of 0.03Ni₂P/CN. Fig. 1f displayed the TEM image of 0.2BV/0.03Ni₂P/CN sample, in which the 0.03Ni₂P/CN as a support was decorated with BiVO₄ decahedron crystals. The HRTEM images of 0.2BV/0.03Ni₂P/CN revealed well-defined lattice fringes of 0.194 and 0.254 nm, corresponding to (204) and (200) planes of BiVO₄ and Ni₂P, respectively (Fig. 1g). Furthermore, small Ni₂P

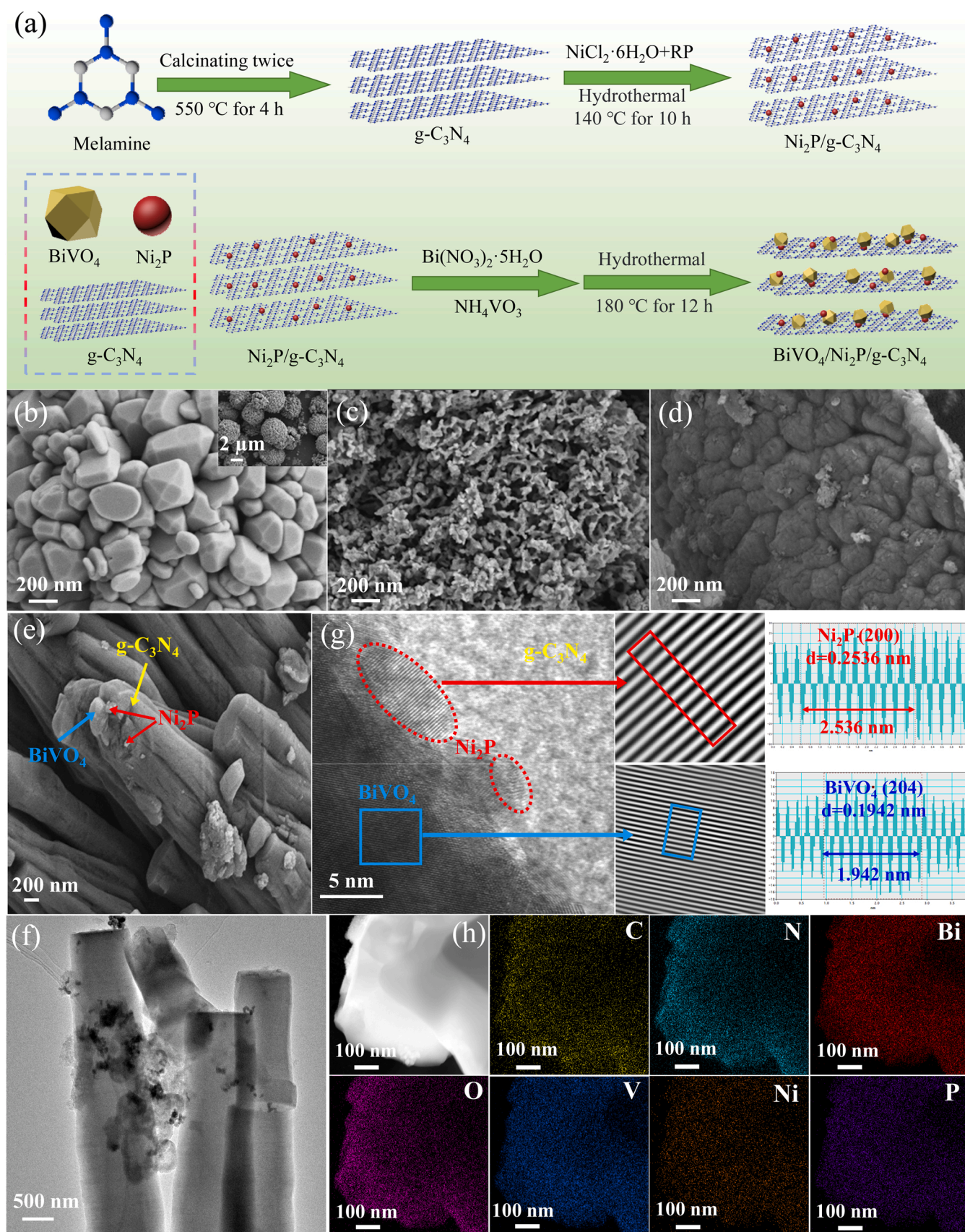


Fig. 1. (a) Preparation procedure of $\text{BiVO}_4/\text{Ni}_2\text{P}/\text{g-C}_3\text{N}_4$; SEM micrographs of (b) BiVO_4 , (c) Ni_2P , (d) $\text{g-C}_3\text{N}_4$ and (e) $0.2\text{BV}/0.03\text{Ni}_2\text{P}/\text{CN}$; (f) TEM image, (g) HRTEM image and (h) elemental mapping images of $0.2\text{BV}/0.03\text{Ni}_2\text{P}/\text{CN}$.

nanoparticle was displayed between BiVO_4 and $\text{g-C}_3\text{N}_4$, which was beneficial to the transfer of photoinduced electrons from BiVO_4 to $\text{g-C}_3\text{N}_4$. Besides, some Ni_2P particles distributed on the surface of $\text{g-C}_3\text{N}_4$, which could not only increase reaction sites, but also reduce the over-potential, thereby heightening photocatalytic properties. To further verify the position of Ni_2P in $\text{BiVO}_4/\text{Ni}_2\text{P}/\text{g-C}_3\text{N}_4$ heterojunction, the electrostatic charge properties of BiVO_4 , Ni_2P and $\text{g-C}_3\text{N}_4$ were measured in neutral solutions through Zeta-potential to study the electrostatic interaction between each other. As exhibited in Fig. S4, the $\text{g-C}_3\text{N}_4$ and BiVO_4 presented negatively charged with the Zeta potential of -13.24 mV and -21.73 mV, respectively. Nevertheless, the Zeta potential of Ni_2P was positively charged about 2.40 mV. Once Ni_2P was deposited on the surface of $\text{g-C}_3\text{N}_4$, a close contact interface could be formed between Ni_2P and $\text{g-C}_3\text{N}_4$ due to strong electrostatic attraction. After further introduction of negatively charged BiVO_4 into $\text{Ni}_2\text{P}/\text{g-C}_3\text{N}_4$ heterojunction, the BiVO_4 preferentially deposited on the positively charged Ni_2P surface of $\text{Ni}_2\text{P}/\text{g-C}_3\text{N}_4$ heterojunction to form $\text{BiVO}_4/\text{Ni}_2\text{P}/\text{g-C}_3\text{N}_4$ heterojunction. The Zeta potential consequence strongly confirmed that Ni_2P was more likely to be electrostatic adsorbed between BiVO_4 and $\text{g-C}_3\text{N}_4$. Furthermore, the corresponding elemental mapping images (Fig. 1h) revealed that all of Bi, V, O, Ni, P, C and N elements evenly dispersed throughout the $0.2\text{BV}/0.03\text{Ni}_2\text{P}/\text{CN}$ photocatalyst.

In addition, TEM and HRTEM images of the $0.2\text{BV}/\text{CN}/0.03\text{Ni}_2\text{P}$ composite were presented in Fig. S5. It can be found that numerous Ni_2P nanoparticles uniformly dispersed on the surface of $0.2\text{BV}/\text{CN}$ sample (Fig. S5a), indicating that no Ni_2P electron-bridge formed between BiVO_4 and $\text{g-C}_3\text{N}_4$. To elucidate the more micro perspective structural information, the HRTEM were carried out. The HRTEM images of $0.2\text{BV}/\text{CN}/0.03\text{Ni}_2\text{P}$ (Fig. S5b) revealed that the (200) plane of Ni_2P with lattice spacing of 0.254 nm was distributed on the surfaces of BiVO_4 and $\text{g-C}_3\text{N}_4$, rather than located between BiVO_4 and $\text{g-C}_3\text{N}_4$. The

above consequence implied that the position of Ni_2P could be effectively regulated by controlling the feeding order.

The crystal structures of the as-prepared catalysts were investigated by XRD analysis. As presented in Fig. S6a, the phase structures of $\text{BiVO}_4/\text{g-C}_3\text{N}_4$ heterojunctions constituted both the hexagonal $\text{g-C}_3\text{N}_4$ (JCPDS: 87–1526) and monoclinic BiVO_4 (JCPDS: 75–1866). Moreover, as the amount of BiVO_4 gradually increased, the characteristic peaks of the $\text{g-C}_3\text{N}_4$ gradually decreased, which confirmed the coexistence of $\text{g-C}_3\text{N}_4$ and BiVO_4 . On the contrary, the characteristic peaks of hexagonal Ni_2P (JCPDS: 74–1385) could not be observed in $\text{BiVO}_4/\text{Ni}_2\text{P}/\text{g-C}_3\text{N}_4$ compounds (Fig. S6b). Despite the amount of Ni_2P was increased to 6 wt%, the diffraction peak of Ni_2P remained undetected, which was primarily attributed to its low content and weak crystallinity. A similar phenomenon appeared in the $0.03\text{Ni}_2\text{P}/\text{CN}$ (Fig. 2a), only the diffraction peak of $\text{g-C}_3\text{N}_4$ could be observed in the $0.03\text{Ni}_2\text{P}/\text{CN}$ complexes.

The optical absorption properties of photocatalysts were recorded by UV–vis DRS spectra, which were delineated in Fig. S7a. Obviously, Ni_2P presented a wider absorption at about $200\text{--}700$ nm, demonstrating that Ni_2P possessed a character of consecutive energy band. Compared to pure $\text{g-C}_3\text{N}_4$, the BiVO_4 presented much stronger visible light absorption properties with an absorption edge at 520 nm. After coupling $\text{g-C}_3\text{N}_4$ with BiVO_4 , the optical absorption of $0.2\text{BV}/\text{CN}$ heterojunction situated between both of them. Moreover, as the loading amount of BiVO_4 increased, the optical absorption edges of $\text{BiVO}_4/\text{g-C}_3\text{N}_4$ gradually red-shifted, which were presented in Fig. S7b. A similar phenomenon appeared on the $\text{Ni}_2\text{P}/\text{g-C}_3\text{N}_4$ (Fig. S7c) and $\text{BiVO}_4/\text{Ni}_2\text{P}/\text{g-C}_3\text{N}_4$ heterojunction (Fig. S7d). In addition, $0.2\text{BV}/0.03\text{Ni}_2\text{P}$ and $0.2\text{BV}/0.03\text{Ni}_2\text{P}/\text{CN}$ composites displayed the combined absorption characters of the homologous components, further demonstrating the coexistence of these phases. Subsequently, the band gap energies (E_g) of BiVO_4 and $\text{g-C}_3\text{N}_4$ were calculated according to Tauc's formula $ah\nu = A(h\nu - E_g)^{n/2}$ [31]. The n values of BiVO_4 and $\text{g-C}_3\text{N}_4$ were taken as 4 owing to the

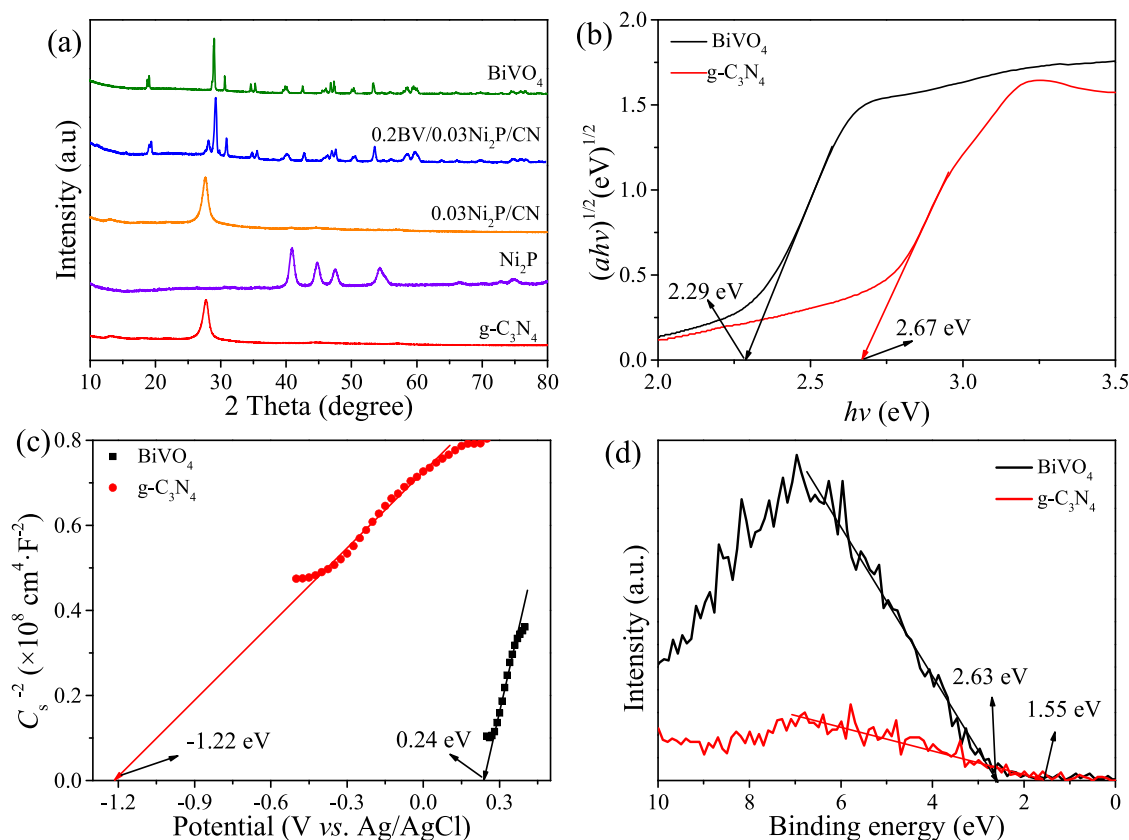


Fig. 2. (a) XRD patterns of the as-obtained samples; (b) Band gap energies, (c) Mott-Schottky (M-S) plots and (d) valence-band XPS (VB-XPS) spectra of BiVO_4 and $\text{g-C}_3\text{N}_4$.

indirect semiconductor character [19,27]. Hence, the E_g values of BiVO_4 and $\text{g-C}_3\text{N}_4$ were 2.29 and 2.67 eV, respectively (Fig. 2b). Besides, the M-S plots (Fig. 2c) were implemented to explore flat-band potentials (E_{fb}) of BiVO_4 and $\text{g-C}_3\text{N}_4$. The positive slopes of the M-S curves implied that they were n type semiconductors. The E_{fb} values of BiVO_4 and $\text{g-C}_3\text{N}_4$ were 0.24 and -1.22 V vs Ag/AgCl (0.44 and -1.02 V vs NHE), respectively [50]. Accordingly, the CB potentials (E_{CB}) of BiVO_4 and $\text{g-C}_3\text{N}_4$ were 0.34 and -1.12 eV, respectively, because the E_{CB} of n -type semiconductor was 0.10 V more negative than that of E_{fb} . The VB potentials (E_{VB}) were calculated to be 2.63 and 1.55 eV according to function $E_{VB} = E_{CB} + E_g$ [50]. Besides, the E_{VB} of BiVO_4 and $\text{g-C}_3\text{N}_4$ were further verified by valence-band XPS (VB-XPS) spectra (Fig. 2d). The E_{VB}

of BiVO_4 and $\text{g-C}_3\text{N}_4$ from the VB-XPS spectra were 2.63 and 1.55 eV, respectively, which were close to those from the M-S plots.

The electronic structures and the correlative density of states (DOS) of BiVO_4 , Ni_2P and $\text{g-C}_3\text{N}_4$ were investigated through DFT calculation. As illustrated in Fig. 3a, the band gap of BiVO_4 was approximately 0.38 eV. In addition, the relevant DOS revealed that the VB was chiefly derived from the O 2p orbital, and the CB was basically contributed by V 3d and Bi 6p state. For $\text{g-C}_3\text{N}_4$ (Fig. 3b), the VB was mainly dominated by N 2p state, which hybridized with a spot of C 2p, while the CB principally consisted of C 2p orbital, which hybridized with trace amounts of N 2p. Nevertheless, Ni_2P displayed a successive energy band (Fig. 3c), which was constituted by P 3p and Ni 3d. In a word, the

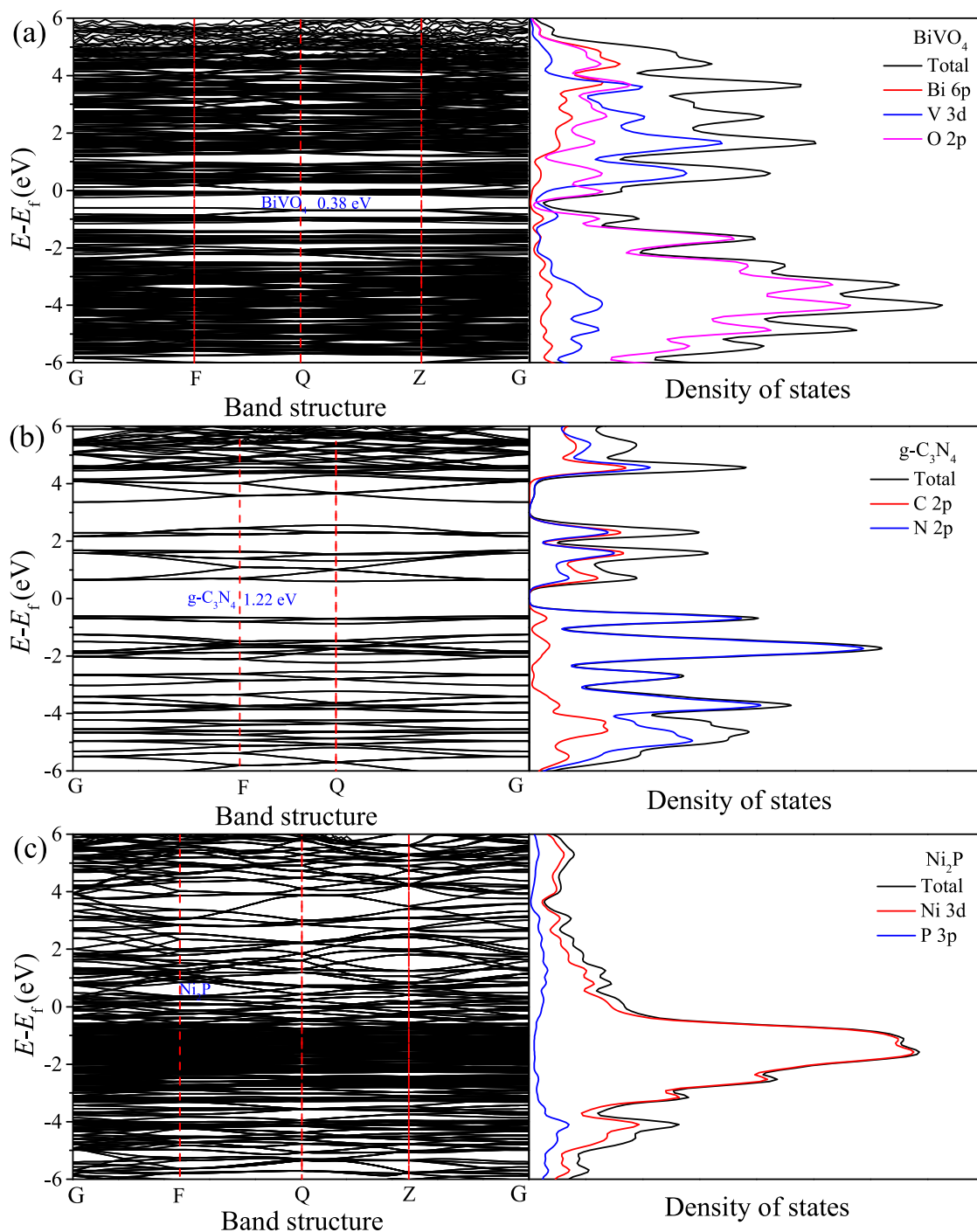


Fig. 3. Calculated band structures and DOS of (a) BiVO_4 , (b) $\text{g-C}_3\text{N}_4$ and (c) Ni_2P .

electrons could occupy the zero-energy level below, rather than the level above in Ni_2P . According to the above consequence, it manifested that introducing Ni_2P surface species into $\text{BiVO}_4/\text{g-C}_3\text{N}_4$ heterojunction not only accelerated the separation of carriers, but also improved the matching relationship between redox potential and energy band structure, thereby boosting available the photocatalytic performance.

3.2. Photo-redox reaction and mechanism of CO_2 reduction with TC removal

Whereafter, the as-obtained photocatalysts were estimated toward CO_2 photoreduction coupled with TC degradation in a cooperative catalytic system under visible light irradiation ($\lambda > 420 \text{ nm}$). As disclosed in Figs. S8a-c, a low photoactivity for CO_2 conversion and TC removal were detected on pristine BiVO_4 and $\text{g-C}_3\text{N}_4$ owing to the swift

recombination of carriers. Notably, after BiVO_4 coupled with $\text{g-C}_3\text{N}_4$, the $\text{BiVO}_4/\text{g-C}_3\text{N}_4$ composites not only triggered the CO_2 conversion, but also accelerated the degradation of TC. Particularly, the 0.2BV/CN heterojunction presented superior photocatalytic activity than that of other samples, illustrating that the construction of heterojunctions effectively accelerated the separation and migration of carriers. Although the construction of the 0.2BV/CN heterojunction could effectively ameliorate the photocatalytic performance, the high interface resistance and limited surficial active sites enormously restricted its actual application. Thus, a difunctional Ni_2P , acting both as an electron-bridge and as a co-catalyst, was introduced into the 0.2BV/CN system to solve the above problems. Subsequently, the effect of difunctional Ni_2P on the photocatalytic activity was probed. As inspected in Figs. S9a-c, with the introduction of difunctional Ni_2P , the photocatalytic activity of ternary 0.2BV/ yNi_2P /CN heterojunctions enhanced steadily until the

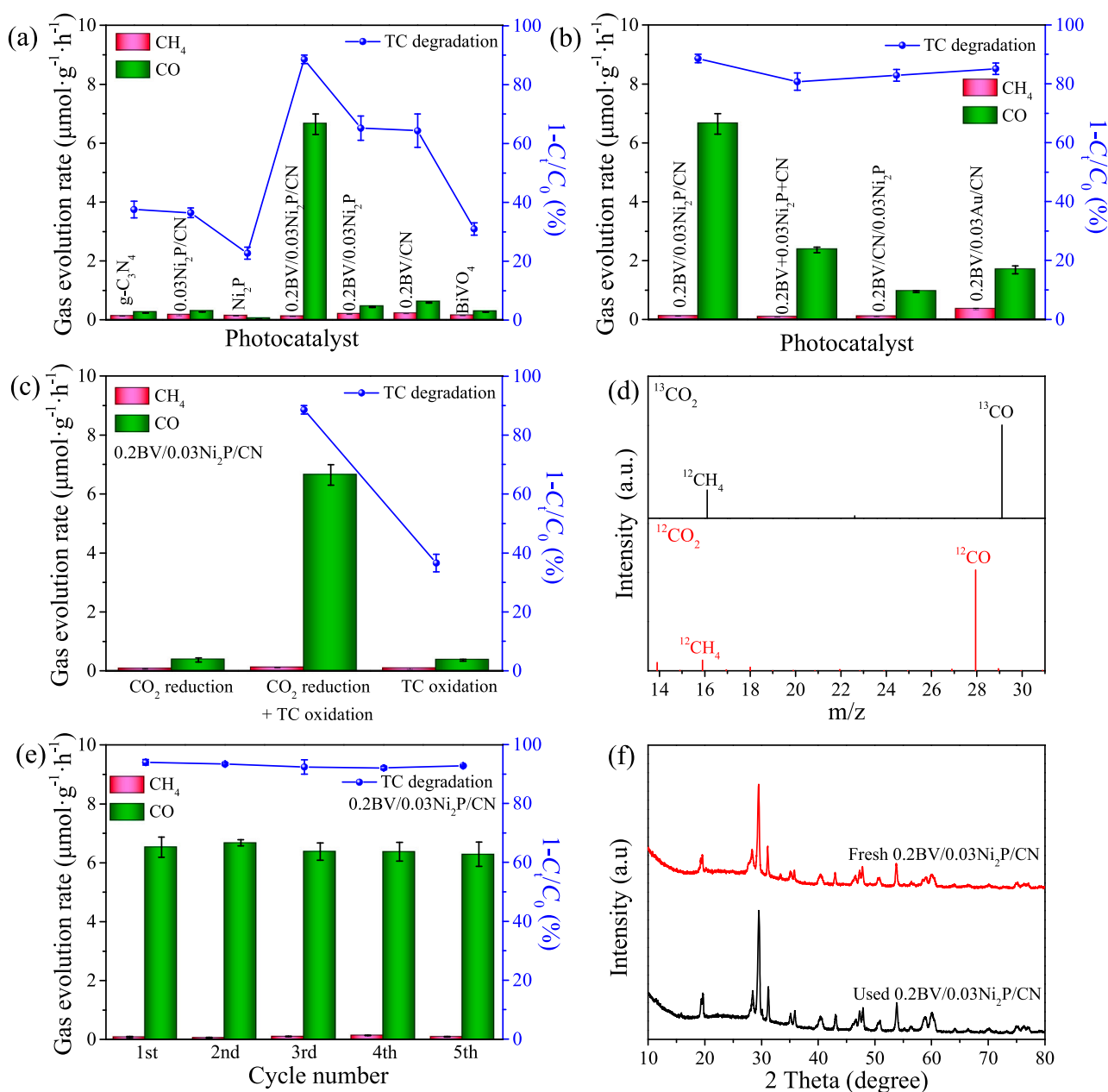


Fig. 4. Gas production rate of (a) bare samples, binary compounds and ternary heterojunctions, and (b) the grinding samples, Ni_2P in different positions and Au electron-bridge for 5 h illumination; (c) Effect of different reaction systems on 0.2BV/0.03Ni₂P/CN; (d) GC-MS patterns of the produced CO and CH₄ over 0.2BV/0.03Ni₂P/CN using ¹²CO₂ and ¹³CO₂ as the carbon source; (e) Cycling runs of 0.2BV/0.03Ni₂P/CN for CO₂ reduction coupled with TC oxidation; (f) XRD patterns of 0.2BV/0.03Ni₂P/CN before and after used.

Ni₂P content reached 3 wt%, nevertheless, as the further increasing the amount of Ni₂P, the photocatalytic activity of the 0.2BV/yNi₂P/CN heterojunctions no longer increased but instead decreased. The above phenomenon was mainly attributed to the fact that despite the addition of difunctional Ni₂P reduced interfacial migration resistance and increased the surface active sites, superfluous Ni₂P could aggregate a large Ni₂P nanocluster size, which was not conducive to the migration and separation of carriers. It is worth noting that the major products CO enormously increased, conversely, the byproducts CH₄ decreased after introduction of Ni₂P into 0.2BV/CN composites. Especially, the 0.2BV/0.03Ni₂P/CN sample presented much superior photocatalytic selectivity towards CO than that of the other photocatalysts, and the selectivity towards CO was 98.31 %, which was 1.31 folds higher than that of binary 0.2BV/CN heterojunction (Table S1). Except for gaseous products, the liquid products such as HCOOH, HCHO, and CH₃OH were also detected. As observed from Figs. S10a-d that no HCHO signal was found in the HPLC spectra, indicating that almost no HCHO was produced during the process of CO₂ photoreduction. Although a small amount of HCOOH and CH₃OH were produced, the yield rate (CH₃OH: 1.2×10^{-5} $\mu\text{mol g}^{-1} \text{h}^{-1}$, HCOOH: 5×10^{-5} $\mu\text{mol g}^{-1} \text{h}^{-1}$) was extremely low, which could be negligible. The above results indicated that the introduction of difunctional Ni₂P not only accelerated the separation and migration of carriers, but also improved the selectivity of CO.

In addition, in contrast with pure samples and binary composites (Fig. 4a and Figs. S11a and b), the ternary 0.2BV/0.03Ni₂P/CN photocatalyst displayed a significant improvement on photocatalytic activity and selectivity, suggesting that the synergistic effect of Ni₂P electron-bridge and co-catalyst played a key role in the photocatalytic CO₂ reduction coupled with TC removal. Upon the cheap Ni₂P was replaced with noble metal Au (Fig. 4b and Figs. S12a and b), the poor photoactivity for CO₂ conversion integrated with TC oxidation occurred on 0.2BV/0.03Au/CN sample, confirming that difunctional Ni₂P, as one of the potential candidates, could effectively modify 0.2BV/CN photocatalyst. An analogous poor photoactivity appeared on 0.2BV/CN/0.03Ni₂P, in which Ni₂P merely acted as a co-catalyst. As expected, the photocatalytic activity of 0.2BV/0.03Ni₂P/CN was significantly superior to that of 0.2BV/CN/0.03Ni₂P, indicating that the Ni₂P as electron-bridge played a leading role compared to the Ni₂P as co-catalyst. Furthermore, it can be seen that the photocatalytic activity of 0.2BV/0.03Ni₂P/CN heterojunction was dramatically higher than that of the mechanical mixture (labeled as 0.2BV+0.03Ni₂P + CN), affirming that the heterojunction structure was indeed formed. Besides, the AQE of the as-prepared photocatalysts were calculated and exhibited in Figs. S13a-c. The AQE of 0.2BV/0.03Ni₂P/CN attained 0.92 % at 420 nm monochromatic light irradiation, which was 13.1, 15.3 and 3.2 times of BiVO₄ (0.07%), g-C₃N₄ (0.06 %) and 0.2BV/CN (0.29 %), respectively. These conclusions delineated that the introducing difunctional Ni₂P could not only accelerate separation and migration of carriers, but also effectively improve the quantum efficiency of BiVO₄/g-C₃N₄.

Apart from the contribution of difunctional Ni₂P, the introduction of TC played also a crucial role in heightening the photocatalytic activity and CO selectivity. As compared to two half-reactions of individual CO₂ photoreduction and independent TC oxidation under Ar atmosphere, such designed coupled reaction system toward CO₂ reduction coupled with TC removal showed much superior catalytic performance and selectivity (Fig. 4c and Figs. S14a and b). As discussed above, the construction of the coupled reaction system was another pivotal role in the enhanced catalytic activity and selectivity. Besides, for independent TC oxidation under Ar atmosphere, a spot of CO and CH₄ were detected, implying that a portion of CO and CH₄ were originated from the decomposition of TC as carbon source. Besides, the ¹³C isotope tracing experiment was implemented over 0.2BV/0.03Ni₂P/CN photocatalyst to track the source of carbon in the coupled reaction system. As delineated in Fig. 4d, only the two peaks at $m/z = 28$ (¹²CO) and $m/z = 16$ (¹²CH₄) in the mass spectra could be discovered using ¹²CO₂ as substrate. Once ¹³CO₂ replaced ¹²CO₂, the peak of ¹³CO ($m/z = 29$) was found,

moreover, some traces of ¹²CH₄ ($m/z = 16$) were also detected, suggesting that the gas products were mainly from CO₂, and only traces were derived from TC mineralization.

Besides, the influence of TC concentration on the selectivity of CO₂ conversion was also probed. As depicted in Figs. S15a-c, the yield rate and selectivity of CO from CO₂ reduction improved steadily until the concentration of TC increased 20 mg/L, nevertheless, as the further addition of TC concentration, the evolution rate and selectivity of CO not any longer enhanced, however, began to descend. This phenomenon ascribed that despite the addition of TC molecules could accelerate the separation of carriers, the higher TC concentration could cover many more reaction sites, resulting in insufficient contact between CO₂ and active sites.

In addition, the other two pollutants, rhodamine B (RhB) and phenol, as common water contaminants, were utilized to investigate the impact of electron donating ability of contaminants on the synergic CO₂ conversion. As displayed in Figs. S16a-c, the introduction of pollutants could heighten the reduction of CO₂. Interestingly, the higher the removal efficiency of TC was, the more favorable to the synergic CO₂ conversion. The outcome could be ascribed to different pollutant molecules with distinct electron donating capability in the coupled system. The above results manifested that TC molecules as electron donors could distinctly enhance the synergistic CO₂ reduction because of TC molecules with high electron-donating capacity.

Photocatalytic cycle practicability and stability of 0.2BV/0.03Ni₂P/CN photocatalyst was assessed via recycling tests (Fig. 4e). Evidently, the photocatalytic activity of 0.2BV/0.03Ni₂P/CN for CO₂ reduction and TC degradation remained comparatively excellent performance after five continuous cycles, demonstrating the good stability of 0.2BV/0.03Ni₂P/CN sample. In addition, the phase structure of 0.2BV/0.03Ni₂P/CN photocatalyst after reaction was measured by XRD patterns (Fig. 4f). Compared with the sample before reaction, almost no change was observed in the used 0.2BV/0.03Ni₂P/CN. Furthermore, the SEM image of 0.2BV/0.03Ni₂P/CN after five cycles was also not much different from that before reaction (Fig. S17). These testified the excellent stability of 0.2BV/0.03Ni₂P/CN photocatalyst during the photocatalytic CO₂ reduction coupled with TC degradation.

Considering that excessive use of catalyst could cause a misleading for cycling results with high conversion rate, the cyclic experiment under lower conversion levels was implemented by lowering the dose of the catalyst to minimize the possibility of catalyst deactivation. It could be observed that the photocatalytic activity of 0.2BV/0.03Ni₂P/CN obviously decreased with the decrease of catalyst dose. Although the overall conversion rate was reduced, it still maintained good and stable photocatalytic performance after five cycles (Fig. S18a). In addition, the crystallographic phase and microstructure of used 0.2BV/0.03Ni₂P/CN photocatalyst were explored by the XRD patterns (Fig. S18b) and SEM (Fig. S18c), respectively. No obvious change could be found in the structure and morphology, implying remarkable stability of 0.2BV/0.03Ni₂P/CN photocatalyst during the photocatalytic reaction.

In order to better understand that the introduction of TC could effectively improve the performance of CO₂ photoreduction in the coupled reaction system, the photocatalytic activity of CO₂ reduction over the reported photocatalysts in the absence of sacrificial agents was summarized in Table 1. The as-obtained 0.2BV/0.03Ni₂P/CN possessed higher catalytic activity for CO₂ photoreduction in the coupled reaction system than that of most reported photocatalysts without sacrificial agents [57–67]. Even though the yield rate of CO and CH₄ reached 9.76 and 6.1 $\mu\text{mol g}^{-1} \text{h}^{-1}$ over g-C₃N₄/Bi₂WO₆ [59] and g-C₃N₄/MXene [67], respectively, close to that of 0.2BV/0.03Ni₂P/CN in this work, either the catalyst dosage was higher or the selectivity of CO was lower than that of this work. Therefore, the as-synthesized 0.2BV/0.03Ni₂P/CN photocatalyst could make a progress for improving quantum efficiency of current catalysts.

Given that the adsorption performance and reactive sites of materials were directly affected by its microstructure. Hence, N₂ sorption

Table 1Comparison the catalytic activity of 0.2BV/0.03Ni₂P/CN to recent reported catalysts for CO₂ reduction.

Sample	Reaction system	Catalyst dose	Light source	Yield rate ($\mu\text{mol g}^{-1} \text{h}^{-1}$)			Refs.
				CH ₄	CO	Selectivity (CO)	
OV-BiOCl/g-C ₃ N ₄	H ₂ O	0.02 g	300 W Xe lamp	0.77	4.73	86.00 %	[57]
ZnIn ₂ S ₄ /BiVO ₄	H ₂ O	0.1 g	300 W Xe lamp	0.09	4.75	98.14 %	[58]
g-C ₃ N ₄ /Bi ₂ WO ₆	H ₂ O	0.1 g	300 W Xe lamp	4.57	5.19	53.17 %	[59]
CPDs/Bi ₁₂ O ₁₇ Cl ₂	H ₂ O	0.03 g	300 W Xe lamp	-	3.21	-	[60]
CdS/BiOI	H ₂ O	0.02 g	300 W Xe lamp	0.18	1.11	86.05 %	[61]
Cd _x Zn _{1-x} S@Au/BiVO ₄	H ₂ O	0.05 g	300 W Xe lamp	-	2.20	-	[62]
Au@Void@g-C ₃ N ₄ /SnS	H ₂ O	0.05 g	300 W Xe lamp	0.95	4.27	81.82 %	[63]
Bi ₂ O ₂ CO ₃ /Bi/Bi ₂ WO ₆	H ₂ O	0.1 g	300 W Xe lamp	2.53	0.81	24.25 %	[64]
BiVO ₄ -Au-Cu ₂ O	H ₂ O	0.1 g	300 W Xe lamp	3.15	2.08	39.77 %	[65]
BiOI/g-C ₃ N ₄	H ₂ O	0.1 g	300 W Xe lamp	0.18	4.86	96.43 %	[66]
g-C ₃ N ₄ /MXene	H ₂ O	0.05 g	300 W Xe lamp	2.12	3.98	65.25 %	[67]
BiVO ₄ /Ni ₂ P/g-C ₃ N ₄	TC and H ₂ O	0.05 g	300 W Xe lamp	0.11	6.40	98.31 %	This work

isotherms of the as-obtained samples were investigated and illustrated in Fig. 5a and Table S2. It is worth noting that the onefold BiVO₄, g-C₃N₄, 0.2BV/CN and 0.2BV/0.03Ni₂P/CN with type IV isotherm revealed the existent of mesoporous structures, which were consistent with the relevant distribution plots of pore size (inserted in Fig. 5a). Furthermore, the Brunauer-Emmett-Teller (BET) surface areas of BiVO₄, g-C₃N₄, 0.2BV/CN and 0.2BV/0.03Ni₂P/CN were calculated to be 2.30, 13.41, 10.38 and 22.07 m² g⁻¹, respectively. Compared with pure g-C₃N₄, the BET surface area of the 0.2BV/CN heterojunction decreased mildly owing to the surface deposition of BiVO₄ with small specific surface area. Once Ni₂P was introduced into 0.2BV/CN heterojunction, the surface area increased from 10.38 m² g⁻¹ to 22.07 m² g⁻¹. This indicated that the introduction of Ni₂P could provide more adsorption sites for photocatalytic CO₂ reduction coupled with TC degradation. To further confirm the above peroration, the CO₂ adsorption isotherms (Fig. 5b) of photocatalysts were carried out. Similar to N₂ adsorption-desorption isotherms, the 0.2BV/0.03Ni₂P/CN photocatalyst possessed a stronger CO₂ adsorption capacity than that of other materials, which was easier to adsorb more CO₂. In addition, the adsorption energies (E_{ads}) of CO₂ on the surface of BiVO₄, Ni₂P, g-C₃N₄, and BiVO₄, g-C₃N₄ or

Ni₂P sides of BiVO₄/Ni₂P/g-C₃N₄ were probed through the DFT calculation (Fig. 5c). Soon afterwards, the E_{ads} values were calculated to be 0.22, -0.51, -0.43, -0.58, -0.78 and -0.91 eV for BiVO₄, Ni₂P, g-C₃N₄, and BiVO₄, g-C₃N₄ or Ni₂P sides of BiVO₄/Ni₂P/g-C₃N₄, respectively. Obviously, the single g-C₃N₄ presented a smaller E_{ads} value than BiVO₄, and a larger E_{ads} value than Ni₂P, demonstrating that g-C₃N₄ had stronger adsorption capacity for CO₂ than BiVO₄, and a weaker adsorption capacity than Ni₂P. What's more, the E_{ads} of BiVO₄ side, g-C₃N₄ side and Ni₂P side for BiVO₄/Ni₂P/g-C₃N₄ were -0.58, -0.78 and -0.91 eV, respectively, illustrating that CO₂ was more likely to adsorb on the co-catalyst Ni₂P side instead of g-C₃N₄ side or BiVO₄ side of BiVO₄/Ni₂P/g-C₃N₄. The above conclusions manifested that the half-reaction of CO₂ reduction was more beneficial to react on the surface of co-catalyst Ni₂P. According to the geometry structures of CO₂ adsorption, it could be observed that CO₂ molecules were mainly adsorbed on Ni atom of co-catalyst Ni₂P, indicating that Ni acted as major adsorption site of CO₂.

In addition, the adsorption of TC on the surface of photocatalyst was also explored according to the adsorption isotherm experiments. As illustrated in Fig. S19, 0.2BV/0.03Ni₂P/CN presented much larger TC

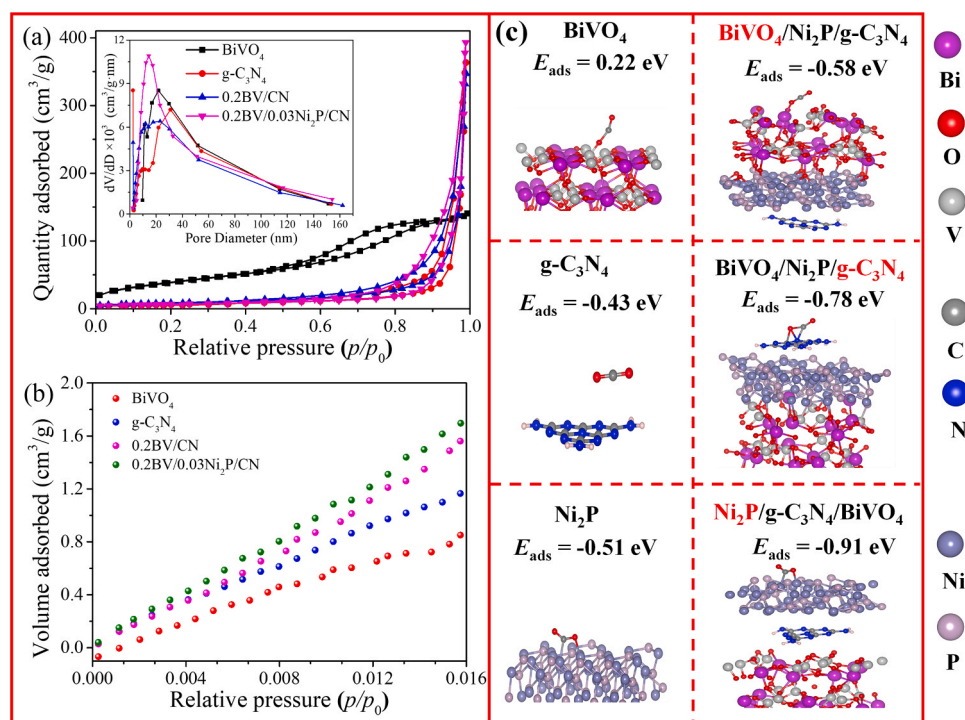
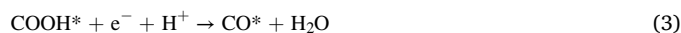


Fig. 5. (a) N₂ adsorption-desorption isotherms and (b) CO₂ adsorption isotherm of the as-obtained samples; (c) Optimized geometry structures and CO₂ adsorption energies on BiVO₄, Ni₂P, g-C₃N₄, and BiVO₄, g-C₃N₄ or Ni₂P sides of BiVO₄/Ni₂P/g-C₃N₄.

adsorption capacity ($q_m = 18.3$ mg/g) than that of $0.03\text{Ni}_2\text{P}/\text{CN}$ ($q_m = 15.6$ mg/g), illustrating that the introduction of BiVO_4 could promote the adsorption of TC. Besides, the adsorption energies (E_{ads}) of TC on BiVO_4 or Ni_2P sides of $\text{BiVO}_4/\text{Ni}_2\text{P}/\text{g-C}_3\text{N}_4$ were calculated through the DFT calculation (Fig. S20) to further confirm the above-mentioned conclusion. It is worth noting that the E_{ads} of BiVO_4 and Ni_2P side for $\text{BiVO}_4/\text{Ni}_2\text{P}/\text{g-C}_3\text{N}_4$ were -2.51 and -1.86 eV, respectively, demonstrating that TC molecule was inclined to adsorb on the BiVO_4 side rather than co-catalyst Ni_2P side of $\text{BiVO}_4/\text{Ni}_2\text{P}/\text{g-C}_3\text{N}_4$. It is worth noting that the holes (h^+) on the BiVO_4 sides of $0.2\text{BV}/0.03\text{Ni}_2\text{P}/\text{CN}$ in this study could oxidize $\text{H}_2\text{O}/\text{OH}^-$ to $\bullet\text{OH}$, which was confirmed by the upcoming discussion of ESR. Therefore, the E_{ads} of H_2O on the surface of BiVO_4 or Ni_2P sides of $\text{BiVO}_4/\text{Ni}_2\text{P}/\text{g-C}_3\text{N}_4$ were also calculated through the DFT calculation to study the specific adsorption sites of TC oxidation (Fig. S21). Compared with Ni_2P sides, the BiVO_4 sides displayed more negative E_{ads} of H_2O , indicating H_2O was more easily adsorbed on the BiVO_4 sides of $\text{BiVO}_4/\text{Ni}_2\text{P}/\text{g-C}_3\text{N}_4$ and then activated to produce $\bullet\text{OH}$. In addition, it could be observed that H_2O molecules were more inclined to adsorb on Bi atoms, and subsequently activated to form $\bullet\text{OH}$ participating in TC oxidation. The above results delineated that Bi as the main adsorption site of TC molecules participated in TC oxidation, whereas, Ni as the major adsorption site of CO_2 participated in CO_2 reduction in the coupled reaction system.

To probe the intermediates of photocatalytic CO_2 conversion coupled with TC oxidation in the coupled reaction system. First of all, the in-situ FT-IR of $0.2\text{BV}/0.03\text{Ni}_2\text{P}/\text{CN}$ sample was conducted to investigate the intermediates of CO_2 reduction. As exhibited in Fig. 6a, with the adsorption of CO_2 species, the monodentate carbonates (m-CO_3^{2-}) were observed at 1684 , 1542 , 1507 and 1472 cm^{-1} and the bidentate carbonates (b-CO_3^{2-}) were found at 1653 and 1337 cm^{-1} , as well as bicarbonate (HCO_3^-) was also discovered at 1419 , 1436 and 1458 cm^{-1} [68]. In addition, several other bidentate formate species (HCOO^-) were also detected at 1558 and 1362 cm^{-1} [69]. Moreover, the peak intensity of HCOO^- species gradually increased with prolonging irradiation time, illustrating that HCOOH was a crucial intermediate in the photocatalytic reduction of CO_2 . Furthermore, the strong band at 1699 cm^{-1} was belonged to the bending vibration of C=O , which descended from the accumulation of CO [70–72]. In addition, the characteristic peaks of

OCH_3^* (1287 cm^{-1}) and OCH_2^* (1339 cm^{-1}) associated with CH_4 generation were much weaker than those of COOH^* [73], which were in accord with their diverse selectivity of product. Whereafter, the calculations of Gibbs free energy of $\text{BiVO}_4/\text{Ni}_2\text{P}/\text{g-C}_3\text{N}_4$ were conducted to further research the reaction route of CO_2 reduction into CO (Fig. 6b-c). According to as-calculated results, the generated COOH^* intermediates were considered as rate-determining step. As delineated in Fig. 6b, the hydrogenation energy of CHO^* ($\Delta G(\text{CHO}^*)$) was apparently higher than the desorption energy of CO molecules ($\Delta G(\text{CO}^*)$). This above result revealed that the CO^* molecules had a tendency to liberate from the surface of $\text{BiVO}_4/\text{Ni}_2\text{P}/\text{g-C}_3\text{N}_4$ as final product, rather than further reduction into CHO^* , which was in line with high selectivity of CO generation. The corresponding reaction pathway was presented in Fig. 6c. Firstly, some CO_2 molecules were adsorbed and activated on the surface of $\text{BiVO}_4/\text{Ni}_2\text{P}/\text{g-C}_3\text{N}_4$ (CO_2^*) and some of them reacted with H_2O molecules to generate H_2CO_3 . In quick succession the H_2CO_3 could ionize to H^+ , HCO_3^- and CO_3^{2-} in reactive system. Next, CO_2^* will react with electron (e^-) and H^+ to form the significant intermediate COOH^* on the surface of $\text{BiVO}_4/\text{Ni}_2\text{P}/\text{g-C}_3\text{N}_4$. Subsequently, COOH^* could be reduced into CO by e^- and H^+ adsorbed on the surface of $\text{BiVO}_4/\text{Ni}_2\text{P}/\text{g-C}_3\text{N}_4$. Finally, the CO molecules could desorb from the surface of $\text{BiVO}_4/\text{Ni}_2\text{P}/\text{g-C}_3\text{N}_4$. Thus, the feasible process of CO_2 photoreduction could be put forward as follows:



Where “*” represented the homologous adsorption state on the surface of photocatalyst.

Whereafter, the intermediate products of TC degradation were detected through LC-MS technique. On the basis of the LC-MS consequence (Fig. S22), the ion at $m/z = 445.1$ was indexed to original TC molecule [74]. The dominating intermediates of TC decomposition were also examined (Figs. S23a-f), whose m/z located at 427.1 , 433.1 , 417.1 , 410.1 , 320.1 , 249.1 , 241.1 , 171.1 , 149.1 and 114.1 , belonging to

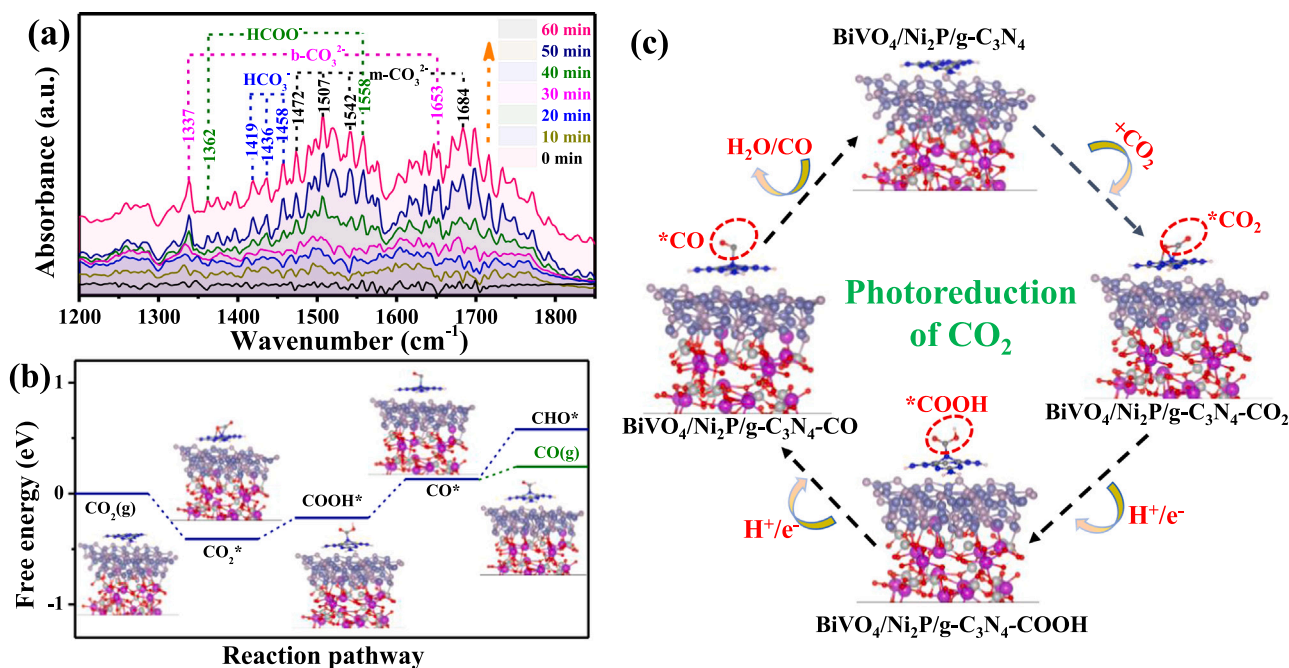


Fig. 6. (a) In situ FTIR spectra of photocatalytic CO_2 reduction over $0.2\text{BV}/0.03\text{Ni}_2\text{P}/\text{CN}$ at different time; (b) Free energy diagrams of $\text{BiVO}_4/\text{Ni}_2\text{P}/\text{g-C}_3\text{N}_4$ during CO_2 reduction; (c) The proposed reaction pathway of CO_2 to CO on $\text{BiVO}_4/\text{Ni}_2\text{P}/\text{g-C}_3\text{N}_4$.

various structures [75–78]. In order to further determine the reliable structure of the aforementioned intermediates, the reactive sites of TC molecules were speculated according to Fukui index by DFT calculation (Fig. 7a-c). It could be observed from Fig. 7b that the highest occupied molecular orbital (HOMO) primarily located on the benzene ring, C1, C8, C11 and C15 atoms of TC molecule. Generally speaking, HOMO located the regions where prefer to lose electrons and are easily oxidized by free radicals [79]. To quantitatively and precisely deduce the reactive sites, the regioselectivity of diverse atoms of TC were presented by calculating Fukui index (Fig. 7c). The most reactive sites of TC molecule were electrophilic attack (f^-) and radical attack (f^0). In other words, the greater f^- or f^0 values signified the stronger reactive sites for the attack by hole (h^+) and $\bullet\text{OH}$. Obviously, C1 ($f^- = 0.031$), C8 ($f^- = 0.0794$) and C11 ($f^- = 0.0308$) presented higher f^- value, meanwhile, C1 ($f^0 = 0.045$), C8 ($f^0 = 0.0472$), C11 ($f^0 = 0.038$), C15 ($f^0 = 0.0293$) and C17 ($f^0 = 0.0271$) possessed higher f^0 value. The above results indicated that C1, C8, C11, C15 and C17 had strong reaction sites, which were more easily oxidized by h^+ and $\bullet\text{OH}$. Soon afterwards, conceivable degradation paths of TC were presented in Fig. S24. Once irradiation, the TC molecule first were attacked by h^+ to form a dehydrated product P1 ($m/z = 427.1$) (Pathway I), which was further oxidized to P2 ($m/z = 410.1$) by opening the benzene ring at the reactive site of C8 ($f^- = 0.0794$ and $f^0 = 0.0472$). Subsequently, radicals attacked the C1 and C11 reactive sites with the large f^0 values to form the product P3 ($m/z = 249.1$), and further produce the P4 ($m/z = 149.1$) and P10 ($m/z = 114.1$) via sequent ring opening and dihydroxylation. Meanwhile, radicals attack on the C15 reactive site of TC molecule with high f^0 value (0.0293) to generate P5 ($m/z = 433.1$) via a ring opening reaction (Pathway II). Whereafter, the C17 reactive site of intermediate P5 was further attacked by h^+ to produce P6 ($m/z = 417.1$), which further was converted to the P7 ($m/z = 320.1$), P8 ($m/z = 241.1$) and P9 ($m/z = 171.1$) via sequent radical-addition, ring opening and decarboxylation reactions. Ultimately, the low-molecular organic substances were further broken down into small inorganic molecules, even were completely mineralized into CO_2 and H_2O . The above conclusions verified that such coupled reaction system was a green, efficient and cyclic reaction system.

3.3. Verification of the Z-Scheme charge transfer

In-situ irradiated XPS, as a pivotal technique, was applied to investigate the valence state of elements and transfer direction of electrons. Fig. S25a exhibited the survey XPS spectra of pristine BiVO_4 , bare $\text{g-C}_3\text{N}_4$, Ni_2P , and 0.2BV/0.03 $\text{Ni}_2\text{P/CN}$, respectively, revealing that C, N, Bi, V, O, Ni and P elements existed in 0.2BV/0.03 $\text{Ni}_2\text{P/CN}$ composite. The detailed high-resolution spectra of C 1s, N 1s, Bi 4f, V 2p, O 1s, Ni 2p and P 2p were presented in Fig. 8a-c and Figs. S25b-e. For C 1s spectra of pristine $\text{g-C}_3\text{N}_4$, the characteristic peak of C 1s at 284.70 eV was attributed to the surface adventitious carbon, and the two peaks at 286.10 and 288.55 eV were related to sp^2 hybridized $\text{N}=\text{C}-\text{N}_2$ (Fig. 8a). Compared to onefold $\text{g-C}_3\text{N}_4$, the peaks of $\text{N}=\text{C}-\text{N}_2$ over the 0.2BV/0.03 $\text{Ni}_2\text{P/CN}$ heterojunction shifted to higher binding energy (BE) (286.34 and 288.57 eV) before illumination and lower BEs (285.80 and 288.35 eV) after illumination, verifying that the C elements of $\text{g-C}_3\text{N}_4$ component in 0.2BV/0.03 $\text{Ni}_2\text{P/CN}$ heterojunction were the electron donor in the dark but electron acceptor in the light. The similar phenomenon occurred in the N 1s in Fig. S25b. For single $\text{g-C}_3\text{N}_4$, the peaks at 397.06, 399.05 and 400.56 eV were assigned to the $\text{C}=\text{N}-\text{C}$, $\text{N}-(\text{C})_3$ and $\text{N}-\text{H}_x$, respectively. The BEs of N 1s peaks in 0.2BV/0.03 $\text{Ni}_2\text{P/CN}$ composite were higher ($\text{C}=\text{N}-\text{C}$: 397.18 eV; $\text{N}-(\text{C})_3$: 399.23 eV; $\text{N}-\text{H}_x$: 400.86 eV) than pure $\text{g-C}_3\text{N}_4$ in the absence of illumination but lower ($\text{C}=\text{N}-\text{C}$: 396.99 eV; $\text{N}-(\text{C})_3$: 398.97 eV; $\text{N}-\text{H}_x$: 400.48 eV) exposed to light, indicating that the N species served as electron donor in darkness but electron acceptor in the light. As seen from Fig. 8b, the BEs of pure BiVO_4 at 164.92 and 159.64 eV corresponded to the Bi 4f_{5/2} and Bi 4f_{7/2} of Bi^{3+} , respectively [31]. After close contact with 0.03 $\text{Ni}_2\text{P/CN}$ in the dark, the BEs (Bi 4f_{5/2}: 164.83 eV; Bi 4f_{7/2}: 159.45 eV) of Bi^{3+} in the 0.2BV/0.03 $\text{Ni}_2\text{P/CN}$ heterojunction lowered relative to the pristine BiVO_4 , conversely, once the 0.2BV/0.03 $\text{Ni}_2\text{P/CN}$ composite was exposed to light, the BEs (Bi 4f_{5/2}: 165.21 eV; Bi 4f_{7/2}: 159.89 eV) of Bi^{3+} increased compared to bare BiVO_4 , illustrating that Bi species was the electron acceptor prior to illumination but electron donor under illumination. Similarly, the BEs of V 2p (Fig. S25c) spectra in 0.2BV/0.03 $\text{Ni}_2\text{P/CN}$ composite displayed a slightly negative shift (V 2p_{1/2}: 524.78 eV; V 2p_{3/2}: 517.21 eV) in darkness and positive shift (V 2p_{1/2}: 525.26 eV; V 2p_{3/2}: 517.49 eV) under illumination in comparison with pristine BiVO_4 (V 2p_{1/2}: 525.01 eV; V 2p_{3/2}: 517.32 eV), implying that the function of V elements was electron donor exposed to light but

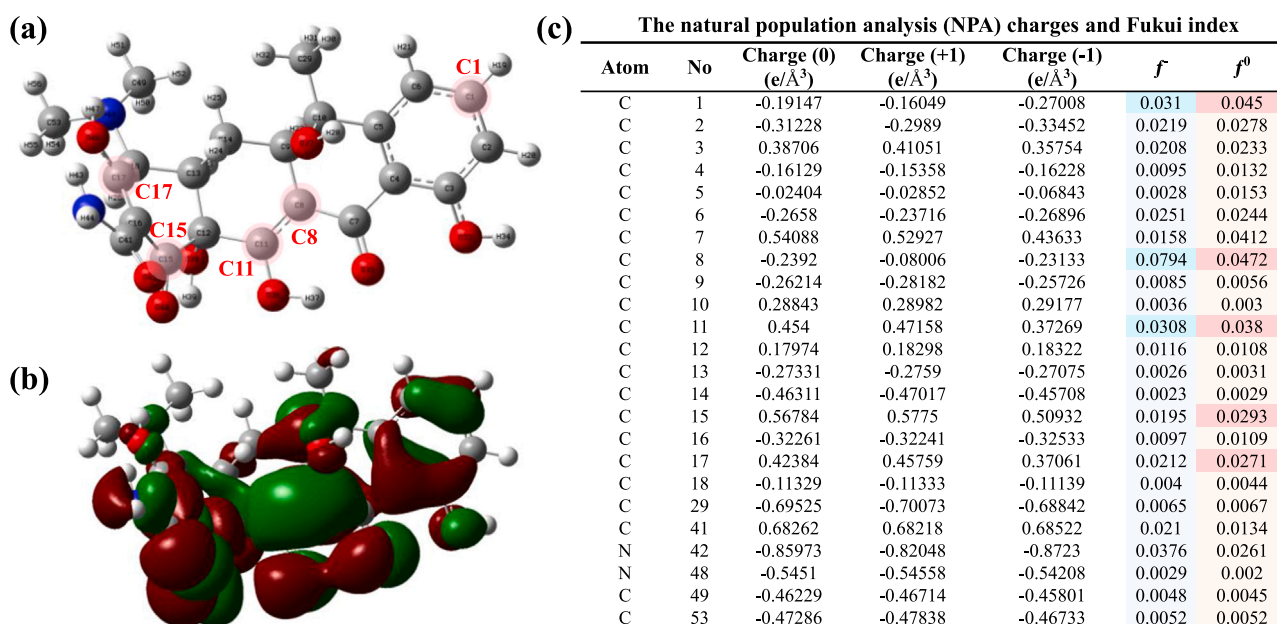


Fig. 7. DFT calculations on TC molecule: (a) Chemical structure; (b) HOMO distributions; (c) NPA charges and calculated Fukui index.

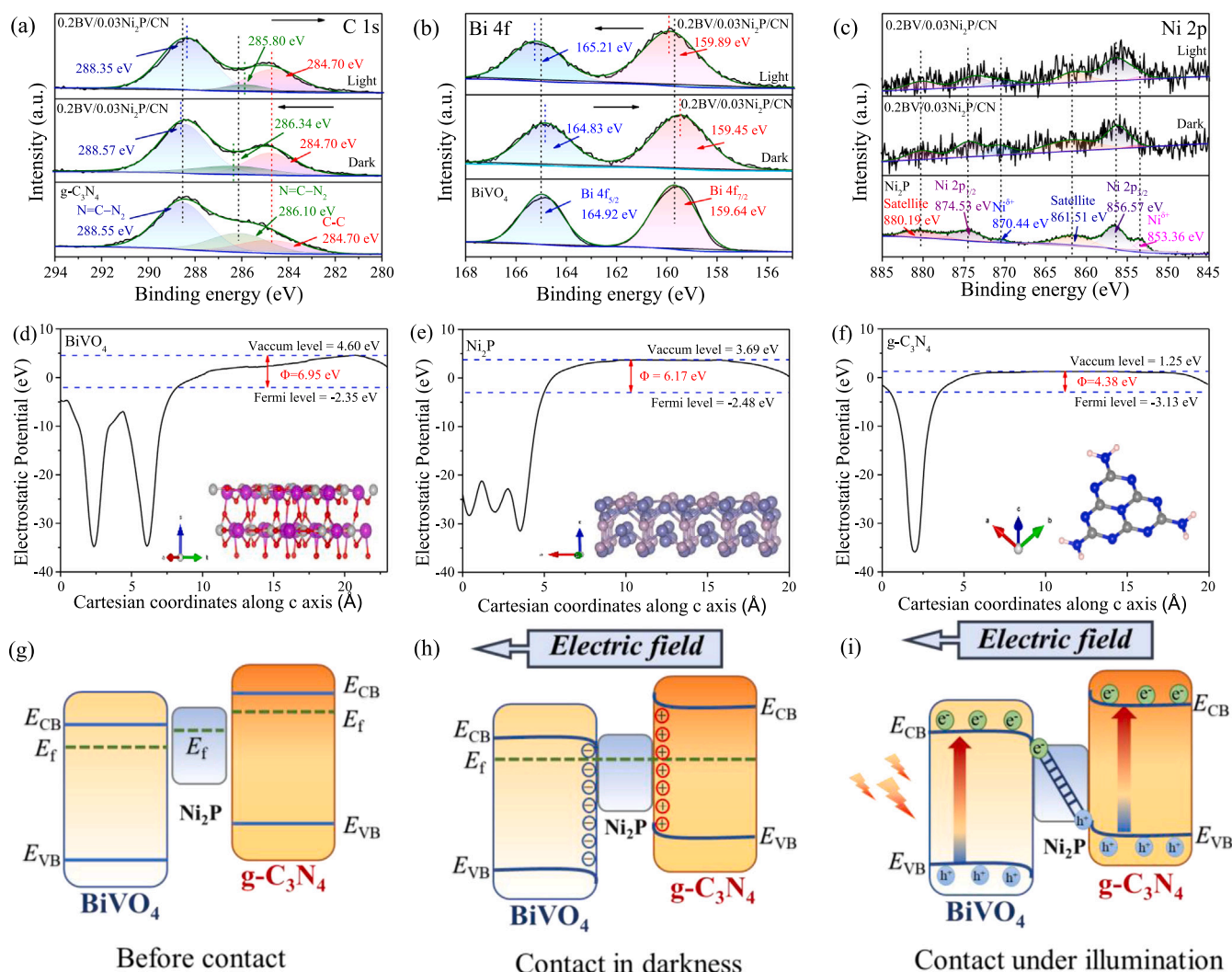


Fig. 8. In-situ XPS high-resolution spectra of (a) C 1s, (b) Bi 4f and (c) Ni 2p of the as-prepared samples with and without illumination; The work function of (d) BiVO₄, (e) Ni₂P and (f) g-C₃N₄; The diagram of electron transfer between BiVO₄ and g-C₃N₄ semiconductor (g) before and (h) after contacted without illumination, and (i) photo-induced carriers migration mechanism in the BiVO₄/Ni₂P/g-C₃N₄ heterojunction under illumination.

electron acceptor prior to illumination. Moreover, the O 1s XPS spectrum (Fig. S25d) of single BiVO₄ could be fitted into two peaks at 530.13 and 531.93 eV, which indexed to the Bi-O bonds and surface-adsorbed hydroxyl groups, respectively [33]. The BEs of Bi-O bonds in the 0.2BV/0.03Ni₂P/CN heterojunction before illumination shifted negatively by 0.06 eV, however, after illumination shifted positively by 0.25 eV with reference to that of pristine BiVO₄. As compared to pristine Ni₂P, the BEs of Ni 2p (Fig. 8c) and P 2p (Fig. S25e) XPS spectra in 0.2BV/0.03Ni₂P/CN composite exhibited no obvious change. However, the peak intensity of Ni 2p correspond to Ni²⁺ or Ni satellite peaks, and P 2p assigned to P³⁻ or PO₄³⁻ in 0.2BV/0.03Ni₂P/CN was weak to some extent due to the low content of Ni₂P in the 0.2BV/0.03Ni₂P/CN heterojunction. This conclusion demonstrated that the e⁻ transferred from g-C₃N₄ to BiVO₄ without illumination but BiVO₄ to g-C₃N₄ within illumination through Ni₂P electron-bridge, indicating that the electrons migration route abided by Z-scheme transfer path.

Subsequently, to explore the transfer direction of electrons in depth, the work functions of BiVO₄, Ni₂P and g-C₃N₄ were calculated by DFT calculation. As illustrated in Fig. 8d-f, the work functions of BiVO₄ (204), Ni₂P (200) and g-C₃N₄ (002) face were 6.95, 6.17 and 4.38 eV, respectively, demonstrating that the Fermi energy (E_f) of Ni₂P was higher than that of BiVO₄, however, lower than that of g-C₃N₄ before contact (Fig. 8g). Once intimate contact without illumination, the

electrons on the CB of g-C₃N₄ spontaneously migrated to Ni₂P, and then flow to BiVO₄ by the heterojunction interface until their E_f reached equilibrium (Fig. 8h). Whereafter, the interface region nearby g-C₃N₄ and BiVO₄ accumulated positive and negative charges, respectively. Because g-C₃N₄ lost electrons and BiVO₄ obtained electrons, leading to the upward and downward bending of band edge for g-C₃N₄ and BiVO₄, respectively. Simultaneously, an internal electric field (IEF) was established between BiVO₄ and g-C₃N₄, which retained the continuous transfer of electrons from g-C₃N₄ to BiVO₄. Upon illumination, the BiVO₄, Ni₂P and g-C₃N₄ were motivated to produce the photo-excited electrons and holes. Soon afterwards, the photoinduced electrons could migrate in the inverse orientation from BiVO₄ to g-C₃N₄, resulting in the Z-scheme migration pathway of electrons (Fig. 8i).

In order to offer more proofs of the Z-scheme transfer channel in BiVO₄/Ni₂P/g-C₃N₄ heterojunction, the chief reactive free radicals, such as •OH and •O₂⁻, were manifested through ESR technique utilizing 5,5-Dimethyl-1-pyrroline N-oxide (DMPO) as trapping agent. It can be seen from Figs. S26a-b that the ESR signals of DMPO•OH and DMPO•O₂⁻ were discovered in the dark. Once exposed to light, the characteristic peaks of DMPO•OH and DMPO•O₂⁻ were observed on BiVO₄ and g-C₃N₄, respectively, and the intensity increased as the light duration increased. Apparently, for pristine BiVO₄, the overt DMPO•OH signal was observed, nevertheless, hardly any DMPO•O₂⁻ signal was detected,

illustrating that the BiVO_4 could produce the $\bullet\text{OH}$ rather than $\bullet\text{O}_2^-$ exposed to light. Contrarily, the $\text{DMPO-}\bullet\text{O}_2^-$ signal was clearly observed but the $\text{DMPO-}\bullet\text{OH}$ signal was hardly found in the simplex $\text{g-C}_3\text{N}_4$, demonstrating that the $\text{g-C}_3\text{N}_4$ could engender $\bullet\text{O}_2^-$ instead of $\bullet\text{OH}$. The above phenomenon was mainly attributed to the fact that the standard reduction potential of $\text{O}_2/\bullet\text{O}_2^-$ (-0.33 V vs NHE) was stronger than that of BiVO_4 (0.34 V vs NHE) but weaker than that of $\text{g-C}_3\text{N}_4$ (-1.12 V vs NHE), meanwhile, the standard oxidation potential of $\text{OH}^-/\bullet\text{OH}$ (1.99 V vs NHE) was weaker than that of BiVO_4 (2.63 V vs NHE) but stronger than that of $\text{g-C}_3\text{N}_4$ (1.55 V vs NHE) [80]. After combining BiVO_4 with $\text{g-C}_3\text{N}_4$, the $\text{DMPO-}\bullet\text{OH}$ and $\text{DMPO-}\bullet\text{O}_2^-$ signals of $0.2\text{BV}/0.03\text{Ni}_2\text{P}/\text{CN}$ were much higher compared with single BiVO_4 with $\text{g-C}_3\text{N}_4$, affirming that the construction of $0.2\text{BV}/0.03\text{Ni}_2\text{P}/\text{CN}$ heterojunction efficaciously expedited the separation rate of charges and thus favored the formation of reaction species. The above verdicts delineated that the reduction sites were located on the surface of $\text{g-C}_3\text{N}_4$ and oxidation sites were situated BiVO_4 side in the $0.2\text{BV}/0.03\text{Ni}_2\text{P}/\text{CN}$ heterojunction through a Z-scheme transfer path, thereby synergistically ameliorating the CO_2 reduction and TC removal in one reaction system.

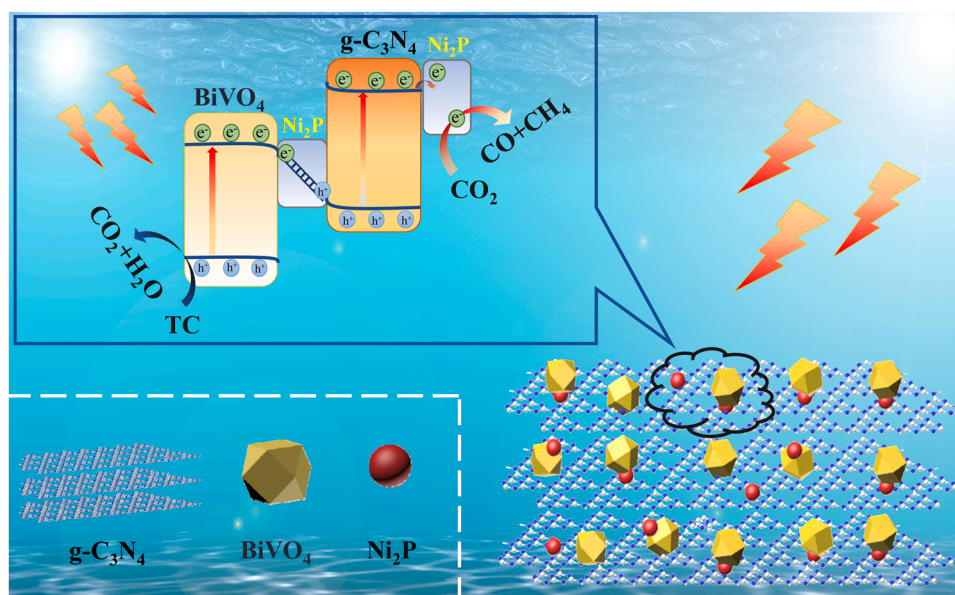
In the light of the above-mentioned analysis, a doable mechanism of reaction over $\text{BiVO}_4/\text{Ni}_2\text{P}/\text{g-C}_3\text{N}_4$ heterojunction was put forward and illustrated in Scheme 1. Once illumination, the BiVO_4 and $\text{g-C}_3\text{N}_4$ were photoexcited to engender the electrons and holes. Whereafter, the relatively weak reduction ability of electrons on CB of BiVO_4 recombined with poor oxidation capability of holes on VB of $\text{g-C}_3\text{N}_4$ via a Ni_2P electron-bridge. Meantime, the strong redox capacity of electrons and holes could be retained on the CB of $\text{g-C}_3\text{N}_4$ and VB of BiVO_4 , respectively. Soon afterwards, a part of electrons on the CB of $\text{g-C}_3\text{N}_4$ could be captured by the Ni_2P cocatalyst and then reduce CO_2 to produce CO and CH_4 , meanwhile, the holes or $\bullet\text{OH}$ on the VB of BiVO_4 participated in the degradation of TC, thereby, actualizing the synergistically photocatalytic CO_2 conversion and TC mineralization. This research further delineated that the introduction of dual-functional TMPs into Z-scheme heterojunction as an effective strategy to realize the coinstantaneous photo-redox reactions.

The transport efficiencies of carriers were inquired by transient photocurrent (TPC) curves of samples. As presented in Fig. 9a, the bare BiVO_4 and $\text{g-C}_3\text{N}_4$ showed weak TPC signals due to the low separation rate of electron-hole pairs. After the combination of each other, the TPC density of $0.2\text{BV}/\text{CN}$ was higher than that of pristine BiVO_4 and $\text{g-C}_3\text{N}_4$, affirming that the construction of Z-scheme heterojunctions availably

accelerated the separation of carriers. Once dual-functional Ni_2P was introduced into the $0.2\text{BV}/\text{CN}$ heterojunction, the $0.2\text{BV}/0.03\text{Ni}_2\text{P}/\text{CN}$ with significant TPC signal compared with the $0.2\text{BV}/\text{CN}$ heterojunction, indicating that the synergistic effect of the Ni_2P electron-bridge and Ni_2P co-catalyst greatly improved the separation and migration of carriers.

In addition, the transfer resistances of charges were elucidated through the EIS spectra in the dark (Fig. 9b). Compared to the pure $\text{g-C}_3\text{N}_4$ and BiVO_4 , the $0.2\text{BV}/\text{CN}$ sample illustrated smaller transfer resistance of carriers, revealing that it owned prominent capability in the transmission process of charges. After the introduction of Ni_2P , the $0.2\text{BV}/0.03\text{Ni}_2\text{P}/\text{CN}$ possessed the smallest arc radius among these photocatalysts, certifying that the dual-functional Ni_2P could enormously depress the interface transfer resistance of $0.2\text{BV}/\text{CN}$, thereby enhancing the separation and migration of charges. Subsequently, the quantitative results were analyzed by fitting the impedance values, which were exhibited in Table S3. Besides, the relevant equivalent circuit was fitted and inserted in Fig. 9b. The fitted R_s values expressed the ohmic resistance between the electrode and catalyst, and the R_p represented the transmission resistance of charges in catalyst. It was unambiguous that the R_s values of different samples presented a small gap, illustrating that close ohmic resistance existed in all catalysts. Instead, the R_p values of Ni_2P , BiVO_4 , $\text{g-C}_3\text{N}_4$, $0.03\text{Ni}_2\text{P}/\text{CN}$, $0.2\text{BV}/0.03\text{Ni}_2\text{P}$, $0.2\text{BV}/\text{CN}$, and $0.2\text{BV}/0.03\text{Ni}_2\text{P}/\text{CN}$ samples exhibited huge diversification, which were 18196, 14478, 12280, 11226, 8074, 6437 and 4788 Ω , respectively. Obviously, the $0.2\text{BV}/0.03\text{Ni}_2\text{P}/\text{CN}$ had the lowest R_p values, certifying that the $0.2\text{BV}/0.03\text{Ni}_2\text{P}/\text{CN}$ heterojunction owned the highest kinetic barrier.

In order to investigate the recombination rate of carriers, the PL spectra were detected and exhibited in Fig. 9c. The pristine $\text{g-C}_3\text{N}_4$ illustrated a high PL intensity, but once combined with the BiVO_4 , the PL signal of $0.2\text{BV}/\text{CN}$ heterojunction availably lowered, demonstrating that the formation of heterojunction could distinctly debase the recombination of electrons and holes. After introducing Ni_2P into $0.2\text{BV}/\text{CN}$ heterojunction, the intensity of $0.2\text{BV}/0.03\text{Ni}_2\text{P}/\text{CN}$ was poor compared to $0.2\text{BV}/\text{CN}$ heterojunction, certifying that the synergistic reaction of difunctional Ni_2P could efficiently restrain the recombination rate of charges. Furthermore, the TRPL decay curves were implement to inquire into the decay lifetimes of charges (Fig. 9d), and the correlative parameters were exhibited in Table S4. The $0.2\text{BV}/0.03\text{Ni}_2\text{P}/\text{CN}$ revealed a longer average lifetime than that of $0.2\text{BV}/\text{CN}$



Scheme 1. Diagrammatic sketch for photocatalytic mechanism of $\text{BiVO}_4/\text{Ni}_2\text{P}/\text{g-C}_3\text{N}_4$ heterojunction.

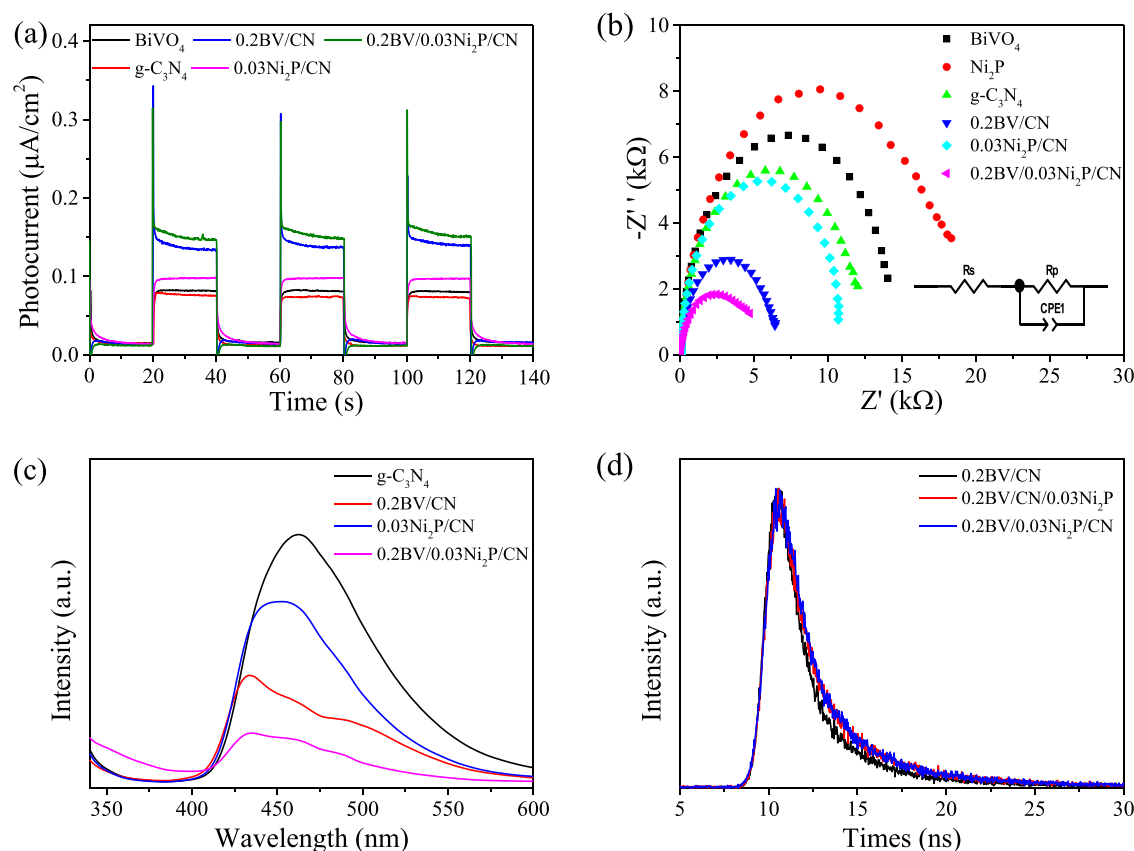


Fig. 9. (a) Photocurrent densities, (b) EIS curves, (c) PL spectra and (d) TRPL decay curves of the as-prepared samples.

and 0.2BV/CN/0.03Ni₂P, illustrating that the synergistic effect of Ni₂P electron-bridge and Ni₂P co-catalysts could help prolong the lifetime of charges. The aforesaid conclusions manifested that the introduced difunctional Ni₂P into the Z-scheme BiVO₄/g-C₃N₄ heterojunction not only expedited the carrier separation and prolonged charge lifetime, but also increased more active sites for participating in redox reactions.

4. Conclusions

In summary, the introduction of a difunctional Ni₂P into BiVO₄/g-C₃N₄ Z-scheme heterojunction was designed and applied in the coupled reaction system for CO₂ reduction integrated with wastewater purification. The synergistic effect of Ni₂P electron-bridge and co-catalyst not only reduced the interfacial migration resistance, but also increased more active sites, thereby maximizing the separation efficiency of carriers for efficient photocatalytic CO₂ reduction coupled with TC degradation. Besides, the coupled reaction system realized the full utilization of the charges, thereby improving the utilization rate of carriers and the photocatalytic activity. Thus, the introduction of difunctional TMPs into heterojunction could supply a doable tactic to capacitate high effective photocatalyst for promising multi-applications in renewable energy generation and environmental remediation.

Declaration of Competing Interest

The authors declare that they have no known competing financial interests or personal relationships that could have appeared to influence the work reported in this paper.

Data availability

Data will be made available on request.

Acknowledgments

This work was financially supported by the National Natural Science Foundation of China (21902056, 22202077, 52272297, 51972134), the Anhui Provincial Natural Science Foundation (1908085MB36), the University Natural Science Research Project of Anhui Province (KJ2021A0522, gxbjZD2021096, 2022AH010030), and the University Synergy Innovation Program of Anhui Province (GXXT-2020-077).

Appendix A. Supporting information

Supplementary data associated with this article can be found in the online version at doi:10.1016/j.apcatb.2023.122957.

References

- [1] L.T. Shi, C.C. Wu, Y. Wang, Y.H. Dou, D. Yuan, H. Li, H.W. Huang, Y. Zhang, I. D. Gates, X.D. Sun, T.Y. Ma, Rational design of coordination bond connected metal organic frameworks/Mxene hybrids for efficient solar water splitting, *Adv. Funct. Mater.* 32 (2022), 2202571.
- [2] X.D. Sun, S.Y. Jiang, H.W. Huang, H. Li, B.H. Jia, T.Y. Ma, Solar energy catalysis, *Angew. Chem. Int. Ed.* 61 (2022), e202204880.
- [3] H.J. Hu, K.L. Zhang, G. Yan, L.T. Shi, B.H. Jia, H.W. Huang, Y. Zhang, X.D. Sun, T. Y. Ma, Precisely decorating CdS on Zr-MOFs through pore functionalization strategy: a highly efficient photocatalyst for H₂ production, *Chin. J. Catal.* 43 (2022) 2332–2341.
- [4] H.W. Huang, J.W. Zhao, Y.J. Du, C. Zhou, M.L. Zhang, Z. Wang, Y.X. Weng, J. Long, J. Hofkens, J.A. Steele, M.B.J. Roelfaers, Direct Z-scheme heterojunction of semicoherent FAPbBr₃/Bi₂WO₆ interface for photoredox reaction with large driving force, *ACS Nano* 14 (2020) 16689–16697.
- [5] N.C. Luo, T. Montini, J. Zhang, P. Fornasiero, E. Fonda, T.T. Hou, W. Nie, J.M. Lu, J.X. Liu, M. Heggen, L. Lin, C.T. Ma, M. Wang, F.T. Fan, S.Y. Jin, F. Wang, Visible-light-driven coproduction of diesel precursors and hydrogen from lignocellulose-derived methylfurans, *Nat. Energy* 4 (2019) 575–584.
- [6] Q. Guo, F. Liang, X.B. Li, Y.J. Gao, M.Y. Huang, Y. Wang, S.G. Xia, X.Y. Gao, Q. C. Gan, Z.S. Lin, C.H. Tung, L.Z. Wu, Efficient and selective CO₂ reduction integrated with organic synthesis by solar energy, *Chem* 5 (2019) 2605–2616.

- [7] Y. Li, F. Gong, Q. Zhou, X.H. Feng, J.J. Fan, Q.J. Xiang, Crystalline isotype heptazine/triazine-based carbon nitride heterojunctions for an improved hydrogen evolution, *Appl. Catal. B* 268 (2020), 118381.
- [8] G. Zhou, Y. Shan, Y.Y. Hu, X.Y. Xu, L.Y. Long, J.L. Zhang, J. Dai, J.H. Guo, J. C. Shen, S. Li, L.Z. Liu, X.L. Wu, Half-metallic carbon nitride nanosheets with microgrid mode resonance structure for efficient photocatalytic hydrogen evolution, *Nat. Commun.* 9 (2018) 3366.
- [9] M.F. Liang, T. Borjigin, Y.H. Zhang, H. Liu, B.H. Liu, H. Guo, Z-scheme Au@Void/g-C₃N₄/SnS yolk-shell heterostructures for superior photocatalytic CO₂ reduction under visible light, *ACS Appl. Mater. Interfaces* 10 (2018) 34123–34131.
- [10] J.D. Li, F. Wei, C.C. Dong, W. Mu, X.J. Han, A Z-scheme ZnFe₂O₄/RGO/In₂O₃ hierarchical photocatalyst for efficient CO₂ reduction enhancement, *J. Mater. Chem. A* 8 (2020) 6524–6531.
- [11] Y. Shen, Q.T. Han, J.Q. Hu, W. Gao, L. Wang, L.Q. Yang, C. Gao, Q. Shen, C.P. Wu, X.Y. Wang, X. Zhou, Y. Zhou, Z.G. Zou, Artificial trees for artificial photosynthesis: construction of dendrite-structured α -Fe₂O₃/g-C₃N₄ Z-Scheme system for efficient CO₂ reduction into solar fuels, *ACS Appl. Energy Mater.* 3 (2020) 6561–6572.
- [12] Y.Y. Wang, H.L. Huang, Z.Z. Zhang, C. Wang, Y.Y. Yang, Q. Li, D.S. Xu, Lead-free perovskite Cs₂AgBiBr₆/g-C₃N₄ Z-scheme system for improving CH₄ production in photocatalytic CO₂ reduction, *Appl. Catal. B* 282 (2021), 119570.
- [13] D.M. Ruan, S. Kim, M. Fujitsuka, T. Majima, Defects rich g-C₃N₄ with mesoporous structure for efficient photocatalytic H₂ production under visible light irradiation, *Appl. Catal. B* 238 (2018) 638–646.
- [14] Y.F. Li, M. Yang, Y. Xing, X.C. Liu, Y. Yang, X. Wang, S.Y. Song, Preparation of carbon-rich g-C₃N₄ nanosheets with enhanced visible light utilization for efficient photocatalytic hydrogen production, *Small* 13 (2017), 1701552.
- [15] J.X. Xu, Y.F. Chen, M. Chen, J. Wang, L. Wang, In situ growth strategy synthesis of single-atom nickel/sulfur co-doped g-C₃N₄ for efficient photocatalytic tetracycline degradation and CO₂ reduction, *Chem. Eng. J.* 442 (2022), 136208.
- [16] H.Y. Tian, X. Liu, Z.Q. Liang, P.Y. Qiu, X. Qian, H.Z. Cui, J. Tian, Gold nanorods/g-C₃N₄ heterostructures for plasmon-enhanced photocatalytic H₂ evolution in visible and near-infrared light, *J. Colloid Interface Sci.* 557 (2019) 700–708.
- [17] L.M. Sun, Y. Qi, C.J. Jia, Z. Jin, W.L. Fan, Enhanced visible-light photocatalytic activity of g-C₃N₄/Zn₂GeO₄ heterojunctions with effective interfaces based on band match, *Nanoscale* 6 (2014) 2649–2659.
- [18] X. Chen, H.K. Li, Y.X. Wu, H.S. Wu, L.D. Wu, P.F. Tan, J. Pan, X. Xiong, Facile fabrication of novel porous graphitic carbon nitride/copper sulfide nanocomposites with enhanced visible light driven photocatalytic performance, *J. Colloid Interface Sci.* 476 (2016) 132–143.
- [19] P. Wen, Y.H. Sun, H. Li, Z.Q. Liang, H.H. Wu, J.C. Zhang, H.J. Zeng, S.M. Geyer, L. Jiang, A highly active three-dimensional Z-scheme ZnO/Au/g-C₃N₄ photocathode for efficient photoelectrochemical water splitting, *Appl. Catal. B* 263 (2020), 118180.
- [20] H.Y. Niu, W.J. Zhao, H.Z. Lv, Y.L. Yang, Y.Q. Cai, Accurate design of hollow/tubular porous g-C₃N₄ from melamine-cyanuric acid supramolecular prepared with mechanochemical method, *Chem. Eng. J.* 411 (2021), 128400.
- [21] F. Dong, Y.J. Sun, M. Fu, Z.B. Wu, S.C. Lee, Room temperature synthesis and highly enhanced visible light photocatalytic activity of porous BiOI/BiOCl composites nanoplates microflowers, *J. Hazard. Mater.* 219–220 (2012) 26–34.
- [22] Q. Sun, Y. Sun, M.Y. Zhou, H.M. Cheng, H.Y. Chen, B. Dorus, M. Lu, T. Le, A 2D/3D g-C₃N₄/ZnO heterojunction enhanced visible-light driven photocatalytic activity for sulfonamides degradation, *Ceram. Int.* 48 (2022) 7283–7290.
- [23] N. Tian, Y.H. Zhang, C.Y. Liu, S.X. Yu, M. Li, H.W. Huang, G-C₃N₄/Bi₄O₅I₂ 2D–2D heterojunctional nanosheets with enhanced visible-light photocatalytic activity, *RSC Adv.* 6 (2016) 10895–10903.
- [24] X.D. Sun, H.W. Huang, Q. Zhao, T.Y. Ma, L.Z. Wang, Thin-layered photocatalysts, *Adv. Funct. Mater.* 30 (2020), 1910005.
- [25] C. Kim, K.M. Cho, A. Al-Saggar, I. Gereige, H.T. Jung, Z-scheme photocatalytic CO₂ conversion on three-dimensional BiVO₄/Carbon-coated Cu₂O nanowire arrays under visible light, *ACS Catal.* 8 (2018) 4170–4177.
- [26] Z.H. Wei, Y.Y. Wang, Y.Y. Li, L. Zhang, H.C. Yao, Z.J. Li, Enhanced photocatalytic CO₂ reduction activity of Z-scheme Cds/BiVO₄ nanocomposite with thinner BiVO₄ nanosheets, *J. CO₂ Util.* 28 (2018) 15–25.
- [27] L. Zou, H.R. Wang, X. Wang, High efficient photodegradation and photocatalytic hydrogen production of Cds/BiVO₄ heterostructure through Z-Scheme process, *ACS Sustain. Chem. Eng.* 5 (2017) 303–309.
- [28] R.H. Zha, C. Li, L. He, M. Zhang, Two-dimensional defective black phosphorus/BiVO₄ nanoheterojunctions for molecular nitrogen activation, *J. Colloid Interface Sci.* 628 (2022) 378–388.
- [29] E. Yalçın, M. Dükkancı, Ternary CuS@Ag/BiVO₄ composite for enhanced photocatalytic and sono-photocatalytic performance under visible light, *J. Solid State Chem.* 313 (2022), 123319.
- [30] C.G. Zhou, S.M. Wang, Z.Y. Zhao, Z. Shi, S.C. Yan, Z.G. Zou, A facet-dependent Schottky-junction electron shuttle in a BiVO₄ (010)-Au-Cu₂O Z-Scheme photocatalyst for efficient charge separation, *Adv. Funct. Mater.* 28 (2018), 181214.
- [31] M. Ou, S.P. Wan, Q. Zhong, S.L. Zhang, Y. Song, L.A. Guo, W. Cai, Y.L. Xu, Hierarchical Z-scheme photocatalyst of g-C₃N₄@Ag/BiVO₄ (040) with enhanced visible-light-induced photocatalytic oxidation performance, *Appl. Catal. B* 221 (2018) 97–107.
- [32] J.J. Wu, L.J. Xiong, Y.J. Hu, Y. Yang, X.Y. Zhang, T.Y. Wang, Z. Tang, A.W. Sun, Y. Zhou, J.Y. Shen, Z.G. Zou, Organic half-metal derived erythroid-like BiVO₄/hm-CaN₃ Z-Scheme photocatalyst: reduction sites upgrading and rate-determining step modulation for overall CO₂ and H₂O conversion, *Appl. Catal. B* 295 (2021), 120277.
- [33] Y.C. Deng, L. Tang, C.Y. Feng, G.M. Zeng, J.J. Wang, Y.Y. Zhou, Y.N. Liu, B. Peng, H.P. Feng, Construction of plasmonic Ag modified phosphorous-doped ultrathin g-C₃N₄ nanosheets/BiVO₄ photocatalyst with enhanced visible-near-infrared response ability for ciprofloxacin degradation, *J. Hazard. Mater.* 344 (2018) 758–769.
- [34] F. Chen, Q. Yang, Y.L. Wang, J.W. Zhao, D.V. Wang, X.M. Li, Z. Guo, H. Wang, Y. C. Deng, C.G. Niu, G.M. Zeng, Novel ternary heterojunction photocatalyst of Ag nanoparticles and g-C₃N₄ nanosheets co-modified BiVO₄ for wider spectrum visible-light photocatalytic degradation of refractory pollutant, *Appl. Catal. B* 205 (2017) 133–147.
- [35] M. Bagherzadeh, R. Kaveha, H. Mahmoudi, Facile synthesis of recyclable Pd-rGO/CNT/CaFe₂O₄ nanocomposite with high multifunctional photocatalytic activities under visible light irradiation, *J. Mater. Chem. A* 7 (2019) 16257–16266.
- [36] Z.L. Jin, Y.K. Zhang, Q.X. Ma, Orthorhombic WP co-catalyst coupled with electron transfer bridge UiO-66 for efficient visible-light-driven H₂ evolution, *J. Colloid Interface Sci.* 556 (2019) 689–703.
- [37] P. Wen, Y.H. Sun, H. Li, Z.Q. Liang, H.H. Wu, J.C. Zhang, H.J. Zeng, S.M. Geyer, L. Jiang, A highly active three-dimensional Z-scheme ZnO/Au/g-C₃N₄ photocathode for efficient photoelectrochemical water splitting, *Appl. Catal. B* 263 (2020), 118180.
- [38] X.Q. Yan, M.Y. Xia, B.R. Xu, J.J. Wei, B.L. Yang, G.D. Yang, Fabrication of novel all-solid-state Z-scheme heterojunctions of 3DOM-WO₃/Pt coated by mono- or few-layered WS₂ for efficient photocatalytic decomposition performance in Vis-NIR region, *Appl. Catal. B* 232 (2018) 481–491.
- [39] Z. Zhao, Y.B. Xing, H.B. Li, P.Y. Peng, Z.C. Sun, Constructing CdS/Cd/doped TiO₂ Z-scheme type visible light photocatalyst for H₂ production, *Sci. China Mater.* 61 (2018) 851–860.
- [40] J. He, D.W. Shao, L.C. Zheng, L.J. Zheng, D.Q. Feng, J.P. Xu, X.H. Zhang, W. C. Wang, W.H. Wang, F. Lu, H. Dong, Y.H. Cheng, H. Liu, R.K. Zheng, Construction of Z-scheme Cu₂O/Cu/AgBr/Ag photocatalyst with enhanced photocatalytic activity and stability under visible light, *Appl. Catal. B* 203 (2017) 917–926.
- [41] J. Wang, Y. Xia, H.Y. Zhao, G.F. Wang, L. Xiang, J.L. Xu, S. Komarneni, Oxygen defects-mediated Z-scheme charge separation in g-C₃N₄/ZnO photocatalysts for enhanced visible-light degradation of 4-chlorophenol and hydrogen evolution, *Appl. Catal. B* 206 (2017) 406–416.
- [42] B.J. Ng, L.K. Putri, L.L. Tan, P. Pasbakhsh, S.P. Chai, All-solid-state Z-scheme photocatalyst with carbon nanotubes as an electron mediator for hydrogen evolution under simulated solar light, *Chem. Eng. J.* 316 (2017) 41–49.
- [43] A. Indra, A. Acharjya, P.W. Menezes, C. Merschjann, D. Hollmann, M. Schwarze, M. Aktas, A. Friedrich, S. Lochbrunner, A. Thomas, M. Driess, Boosting visible-light-driven photocatalytic hydrogen evolution with an integrated nickel phosphide-carbon nitride system, *Angew. Chem. Int. Ed.* 56 (2017) 1653–1657.
- [44] E.J. Popczun, J.R. McKone, C.G. Read, A.J. Baciocchi, A.M. Wiltrout, N.S. Lewis, R. E. Schaak, Nanostructured nickel phosphide as an electrocatalyst for the hydrogen evolution reaction, *J. Am. Chem. Soc.* 135 (2013) 9267–9270.
- [45] Z.J. Sun, H.F. Zheng, J.S. Li, P.W. Du, Extraordinarily efficient photocatalytic hydrogen evolution in water using semiconductor nanorods integrated with crystalline Ni₂P cocatalysts, *Energy Environ. Sci.* 8 (2015) 2668–2676.
- [46] R.C. Shen, J. Xie, Q.J. Xiang, X.B. Chen, J.Z. Jiang, X. Li, Ni-based photocatalytic H₂-production cocatalysts, *Chin. J. Catal.* 40 (2019) 240–288.
- [47] X.L. Li, X.J. Wang, J.Y. Zhu, Y.P. Li, J. Zhao, F.T. Li, Fabrication of two-dimensional Ni₂P/ZnIn₂S₄ heterostructures for enhanced photocatalytic hydrogen evolution, *Chem. Eng. J.* 353 (2018) 15–24.
- [48] D.S. Dai, L. Wang, N. Xiao, S.S. Li, H. Xu, S. Liu, B.R. Xu, D. Lv, Y.Q. Gao, W. Y. Song, L. Ge, J. Liu, In-situ synthesis of Ni₂P co-catalyst decorated Zn_{0.5}Cd_{0.5}S nanorods for high quantum-yield photocatalytic hydrogen production under visible light irradiation, *Appl. Catal. B* 233 (2018) 194–201.
- [49] H. He, J. Cao, M.N. Guo, H.L. Lin, J.F. Zhang, Y. Chen, S.F. Chen, Distinctive ternary Cds/Ni₂P/g-C₃N₄ composite for overall water splitting: Ni₂P accelerating separation of photocarriers, *Appl. Catal. B* 249 (2019) 246–256.
- [50] N.N. Chen, X.M. Jia, H. He, H.L. Lin, M.N. Guo, J. Cao, J.F. Zhang, S.F. Chen, Promoting photocarriers separation in S-scheme system with Ni₂P electron bridge: the case study of BiOBr/Ni₂P/g-C₃N₄, *Chin. J. Catal.* 43 (2022) 276–287.
- [51] X.Y. Lu, J. Xie, X.B. Chen, X. Li, Engineering MPx (M = Fe, Co or Ni) interface electron transfer channels for boosting photocatalytic H₂ evolution over g-C₃N₄/MoS₂ layered heterojunctions, *Appl. Catal. B* 252 (2019) 250–259.
- [52] S.E. Braslavsky, A.M. Braun, A.E. Cassano, A.V. Emeline, M.I. Litter, L. Palmisano, V.N. Parmon, N. Serpone, Glossary of terms used in photocatalysis and radiation catalysis (IUPAC Recommendations 2011), *Pure Appl. Chem.* 83 (2011) 931–1014.
- [53] G. Kresse, J. Furthmüller, Efficient iterative schemes for ab initio total-energy calculations using a plane-wave basis set, *Phys. Rev. B* 54 (1996) 11169–11186.
- [54] G. Kresse, D. Joubert, From ultrasoft pseudopotentials to the projector augmented-wave method, *Phys. Rev. B* 59 (1999) 1758.
- [55] J.P. Perdew, J.A. Chevary, S.H. Vosko, K.A. Jackson, M.R. Pederson, D.J. Singh, C. Fiolhais, Atoms, molecules, solids, and surfaces: applications of the generalized gradient approximation for exchange and correlation, *Phys. Rev. B* 46 (1992) 6671–6687.
- [56] J.P. Perdew, K. Burke, M. Ernzerhof, Generalized gradient approximation made simple, *Phys. Rev. Lett.* 77 (1996) 3865–3868.
- [57] Y. Chen, F. Wang, Y.H. Cao, F.Y. Zhang, Y.Z. Zou, Z. Huang, L.Q. Ye, Y. Zhou, Interfacial oxygen vacancy engineered two-dimensional g-C₃N₄/BiOCl heterostructures with boosted photocatalytic conversion of CO₂, *ACS Appl. Energy Mater.* 3 (2020) 4610–4618.
- [58] Q.T. Han, L. Li, W. Gao, Y. Shen, L. Wang, Y.T. Zhang, X.Y. Wang, Q. Shen, Y. J. Xiong, Y. Zhou, Z.G. Zou, Elegant construction of ZnIn₂S₄/BiVO₄ hierarchical

- heterostructures as direct Z-scheme photocatalysts for efficient CO₂ photoreduction, *ACS Appl. Mater. Interfaces* 13 (2021) 15092–15100.
- [59] M.L. Li, L.X. Zhang, X.Q. Fan, Y.J. Zhou, M.Y. Wu, J.L. Shi, Highly selective CO₂ photoreduction to CO over g-C₃N₄/Bi₂WO₆ composites under visible light, *J. Mater. Chem. A* 3 (2015) 5189–5196.
- [60] Y. Quan, B. Wang, G.P. Liu, H.M. Li, J.X. Xia, Carbonized polymer dots modified ultrathin Bi₁₂O₁₇Cl₂ nanosheets Z-scheme heterojunction for robust CO₂ photoreduction, *Chem. Eng. Sci.* 232 (2021), 116338.
- [61] R.H. Zhou, Z.H. Wei, Y.Y. Li, Z.J. Li, H.C. Yao, Construction of visible light responsive Z-scheme CdS/BiOI photocatalyst with enhanced photocatalytic CO₂ reduction activity, *J. Mater. Res.* 34 (2019) 3907–3917.
- [62] J.K. Li, W.F. Shao, M. Geng, S.P. Wan, M. Ou, Y.H. Chen, Combined Schottky junction and doping effect in Cd₃Zn_{1-x}S@Au/BiVO₄ Z-scheme photocatalyst with boosted carriers charge separation for CO₂ reduction by H₂O, *J. Colloid Interface Sci.* 606 (2022) 1469–1476.
- [63] M.F. Liang, T. Borjigin, Y.H. Zhang, H. Liu, B.H. Liu, H. Guo, Z-scheme Au@Void@g-C₃N₄/SnS yolk-shell heterostructures for superior photocatalytic CO₂ reduction under visible light, *ACS Appl. Mater. Interfaces* 10 (2018) 34123–34131.
- [64] Y.Y. Zhang, L.L. Wang, F.Y. Dong, Q. Chen, H.Y. Jiang, M. Xu, J.S. Shi, Non-additional carbon source one-step synthesis of Bi₂O₂CO₃-based ternary composite for efficient Z-scheme photocatalysis, *J. Colloid Interface Sci.* 536 (2019) 575–585.
- [65] C.G. Zhou, S.M. Wang, Z.Y. Zhao, Z. Shi, S.C. Yan, Z.G. Zou, A facet-dependent Schottky junction electron shuttle in a BiVO₄{010}-Au-Cu₂O Z-scheme photocatalyst for efficient charge separation, *Adv. Funct. Mater.* 28 (2018) 1801214.
- [66] J.C. Wang, H.C. Yao, Z.Y. Fan, L. Zhang, J.S. Wang, S.Q. Zang, Z.J. Li, Indirect Z-scheme BiOI/g-C₃N₄ photocatalysts with enhanced photoreduction CO₂ activity under visible light irradiation, *ACS Appl. Mater. Interfaces* 8 (2016) 3765–3775.
- [67] X. Li, Y. Bai, X. Shi, J.D. Huang, K. Zhang, R. Wang, L.Q. Ye, Mesoporous g-C₃N₄/MXene (Ti₃C₂T_x) heterojunction as a 2D electronic charge transfer for efficient photocatalytic CO₂ reduction, *Appl. Surf. Sci.* 546 (2021), 149111.
- [68] J. Di, C. Chen, C. Zhu, R. Long, H.L. Chen, X.Z. Cao, J. Xiong, Y.X. Weng, L. Song, S. Z. Li, H.M. Li, Y.J. Xiong, Z. Liu, Surface local polarization induced by bismuth-oxygen vacancy pairs tuning non-covalent interaction for CO₂ photoreduction, *Adv. Energy Mater.* 11 (2021), 2102389.
- [69] B. Wang, W. Zhang, G.P. Liu, H.L. Chen, Y.X. Weng, H.M. Li, P.K. Chu, J.X. Xia, Excited electron-rich Bi^{(3-x)+} sites: A quantum well-like structure for highly promoted selective photocatalytic CO₂ reduction performance, *Adv. Funct. Mater.* 32 (2022), 2202885.
- [70] L.J. Liu, Y.Q. Jiang, H.L. Zhao, J.T. Chen, J.L. Cheng, K.S. Yang, Y. Li, Engineering coexposed 001 and 101 facets in oxygen-deficient TiO₂ nanocrystals for enhanced CO₂ photoreduction under visible light, *ACS Catal.* 6 (2016) 1097–1108.
- [71] H. Zhao, L. Liu, J.M. Andino, Y. Li, Bicrystalline TiO₂ with controllable anatase-brookite phase content for enhanced CO₂ photoreduction to fuels, *J. Mater. Chem. A* 1 (2013) 8209–8216.
- [72] S.W. Cao, Y. Li, B.C. Zhu, M. Jaroniec, J.G. Yu, Facet effect of Pd cocatalyst on photocatalytic CO₂ reduction over g-C₃N₄, *J. Catal.* 349 (2017) 208–217.
- [73] S.Q. Gong, Y.L. Niu, X. Teng, X. Liu, M.Z. Xu, C. Xu, T.J. Meyer, Z.F. Chen, Visible light-driven, selective CO₂ reduction in water by In-doped Mo₂C based on defect engineering, *Appl. Catal. B* 310 (2022), 121333.
- [74] Q. Wang, H.M. Zhu, B. Li, Synergy of Ti-O-based heterojunction and hierarchical 1D nanobelt/3D microflower heteroarchitectures for enhanced photocatalytic tetracycline degradation and photoelectrochemical water splitting, *Chem. Eng. J.* 378 (2019), 122072.
- [75] X.N. Wang, J.P. Jia, Y.L. Wang, Combination of photocatalysis with hydrodynamic cavitation for degradation of tetracycline, *Chem. Eng. J.* 315 (2017) 274–282.
- [76] Z.H. Li, X.L. Wang, N.N. Xu, Y. Xiao, L.L. Ma, J.Y. Duan, Cost-effective and visible-light driven melamine-derived sponge for tetracyclines degradation and *Salmonella* inactivation in water, *Chem. Eng. J.* 394 (2020), 124913.
- [77] Z.L. Li, C.S. Guo, J.C. Lyu, Z. Hu, M. Ge, Tetracycline degradation by persulfate activated with magnetic Cu/CuFe₂O₄ composite: efficiency, stability, mechanism and degradation pathway, *J. Hazard. Mater.* 373 (2019) 85–96.
- [78] J.C.E. Yang, Y. Lin, H.H. Peng, B. Yuan, D.D. Dionysiou, X.D. Huang, D.D. Zhang, M.L. Fu, Novel magnetic rod-like Mn-Fe oxycarbide toward peroxymonosulfate activation for efficient oxidation of butyl paraben: radical oxidation versus singlet oxygenation, *Appl. Catal. B* 268 (2020), 118549.
- [79] D.L. Huang, Q. Zhang, C. Zhang, R.Z. Wang, R. Deng, H. Luo, T. Li, J. Li, S. Chen, C. H. Liu, Mn doped magnetic biochar as persulfate activator for the degradation of tetracycline, *Chem. Eng. J.* 391 (2020), 123532.
- [80] X.M. Jia, Q.F. Han, H.Z. Liu, S.Z. Li, H.P. Bi, A dual strategy to construct flowerlike S-scheme BiOBr/BiOAc_{1-x}Br_x heterojunction with enhanced visible-light photocatalytic activity, *Chem. Eng. J.* 399 (2020), 125701.